TECHNISCHE UNIVERSITÄT WIEN

VIENNA UNIVERSITY OF TECHNOLOGY

DIPLOMARBEIT

Laser-cluster interaction - production of hot electrons by short laser pulses

ausgeführt am

Institut für Theoretische Physik
der Technischen Universität Wien

Institute for Theoretical Physics
Vienna University of Technology

unter der Anleitung von
O.Univ.Prof. Dipl.-Phys. Dr.rer.nat. Joachim Burgdörfer
und
Vertr.Ass. Dipl.-Ing. Nina Rohringer

durch

Cornelia Deiss
Rechte Wienzeile 9/3
1040 Wien
cornelia@concord.itp.tuwien.ac.at

Contents

Chapter 1

Introduction

The interaction of short and ultra-short laser pulses with clusters has become a broad area of research over the past ten years. When it comes to the emission of x-ray radiation from laser-induced plasmas, rare gas clusters combine the advantages of solid and gaseous targets. Like solids, they provide large x-ray yields, yet they are debris-free, just like gaseous targets. Characteristic x-ray radiation produced by K, L and M shell vacancies has been observed for argon and krypton clusters[1, 2]. L and M shell emission could be obtained with xenon clusters. The clusters are irradiated by laser pulses with pulse lengths ranging from several femtoseconds to a few picoseconds and intensities from $\sim 10^{15}\mathrm{Wcm}^{-2}$ up to $\sim 10^{18}\mathrm{Wcm}^{-2}$. The strong laser field ionizes the atoms in the cluster and the quasi-free electrons in the cluster are accelerated. If the electrons are heated up sufficiently, inner shell vacancies in the cluster atoms can be created be electron impact ionization. These vacancies are the origin of the measured characteristic x-ray radiation. As the electrons in the clusters are heated up, some of them will eventually leave the cluster, thus causing the build-up of an overall charge of the cluster. This eventually leads to the Coulomb explosion of the cluster. As the cluster expands rapidly, the probability for electron impact ionization of the cluster atoms drops dramatically, and the emission of x-rays ceases. This specific feature of cluster targets could possibly be used for the production of ultrashort x-ray sources. The analysis of the x-ray emission also gives valuable information about the evolution of the plasma inside the cluster, as the production of inner shell vacancies is directly linked to the electron dynamics. Although there are many theoretical studies of the plasma dynamics in clusters [3, 4, 5, 6, 7, 8, 9, 10], there is to date a lack of quantitative predictions for x-ray yields.

Recent experiments [2, 11, 12, 13] show an unexpectedly low laser intensity threshold for the production of x-ray radiation. The mean energy a

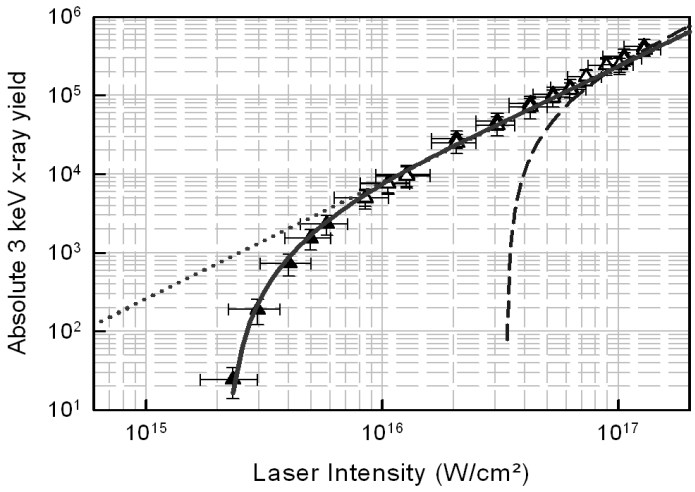

Figure 1.1: *Evolution of the x-ray yield with the laser intensity for an argon cluster [12]. The intensity threshold for the x-ray production lies at* $I_{th} \approx 2.0 \cdot 10^{15}\mathrm{Wcm}^{-2}$. *The dashed line indicates the threshold that would correspond to the intensity where the ponderomotive energy is higher than the K-shell binding energy.*

free electron acquires in an oscillating laser field of amplitude F is called the ponderomotive energy and is given (in atomic units) by:

$$U_P = \frac{F^2}{4\omega^2}. \tag{1.1}$$

At first glance, the electrons in the cluster appear to be mainly accelerated by the laser field. One would therefore expect a threshold for the production of inner shell vacancies by electron impact ionization, that would correspond to the laser intensity, where the ponderomotive energy of the electrons in the field is equal to the ionization energy of the bound inner shell electrons. For argon K-shell electrons, the binding energy is $\sim$ 3keV, thus suggesting an intensity threshold at $I_{th} \approx 3.5 \cdot 10^{16}\mathrm{Wcm}^{-2}$. Surprisingly, first experiments found a threshold intensity as low as $I_{th} \approx 2.0 \cdot 10^{15}\mathrm{Wcm}^{-2}$ (fig. 1.1) for clusters with $N \approx 2.8 \cdot 10^5$ argon atoms and for pulses with a wavelength $\lambda = 800$nm and a length of $\tau = 60$fs (at full width half maximum, FWHM). For this laser intensity the ponderomotive energy is of the order of $U_P \simeq 75$eV, more than one order of magnitude below the energy threshold for K-shell electron-impact ionization of argon. The threshold can be even

lower for longer pulses durations. The value of the threshold depends on the characteristics of the laser (wavelength and pulse length) as well as of the clusters (cluster size and atomic species). These experiments show clearly that additional heating mechanisms are at play inside the cluster.

The underlying physics of the efficient electron heating to energies well above U_P within only $\sim$ 20 optical cycles has not yet been convincingly explained by any theory. There are different theoretical approaches to the study of electron acceleration mechanisms in clusters. In the nanoplasma model a quasi-resonant absorption was proposed [3] that assumed a matching of the laser frequency and the plasma frequency of the electron plasma. The quantitative conclusions drawn from this model are not in agreement with the experimental results and the model can not explain the low intensity threshold for x-ray production [12]. As we will discuss in chapter 7, because of the short duration of the laser pulse (FWHM $\tau \simeq$ 60fs or $\sim$ 24 optical cycles) and the high density of the plasma, the resonance condition is only fulfilled in certain parameter ranges. Alternatively, for small clusters (up to $\sim$ 1000 atoms) a quasi-resonant periodic reflection of electrons at the cluster boundaries was suggested[4, 5]. Such a mechanism seems unrealistic for large cluster sizes and low laser intensities as the time to travel across the cluster becomes much larger than the laser period. Molecular dynamic simulations [6, 7, 8] are limited to about 1000 atoms and results obtained for small clusters are difficult to scale to larger sizes. The focus of many of these simulations was primarily on the charge state and the expansion[6, 8]. The recently proposed microscopic particle in cell method [9] reaches clusters of 25000 atoms and proposes a dephasing between the dipole moment of the cluster and the laser field as heating mechanism. However as the simulation runs are very long (several weeks for one configuration), no detailed study of the parameters has yet been done.

In this work we examine a new pathway to efficient heating so far not considered or, by the way of unrealistic choices for core potentials [5, 8, 7], underestimated in previous simulations: an electron can gain kinetic energy in the laser field well beyond the ponderomotive energy within a few optical cycles if its velocity vector is always aligned with the field vector (see figure 1.2). Flipping the electron velocity vector as the electric field changes direction every half-cycle can occur by backscattering at ionic cores in the cluster. This process can be viewed as a close relative to the Fermi shuttle acceleration [14, 15] where the ionic core plays the role of the stationary wall while the laser field plays the part of the moving wall. Elastic electron ion scattering was neglected in some of the previous models [4, 10] based on the argument that the mean-free path for elastic scattering, $\lambda_e = (n\sigma_e)^{-1}$ (σ_e: elastic electron-ion scattering cross-section), exceeds, for small clusters, the

cluster diameter D. However for large clusters $\lambda_e \lesssim D$. Other simulations employing unrealistic core potentials such as softened Coulomb potentials fail to capture the influence of the relatively large probability for large-angle scattering $\frac{d\sigma_e}{d\theta}$ ($\theta > 90°$) essential for efficiently flipping the direction of the velocity vector. The importance of the choice of the ionic scattering potential has also been discussed in Ref. [16] for the case of vacuum ultraviolet (VUV) laser pulses.

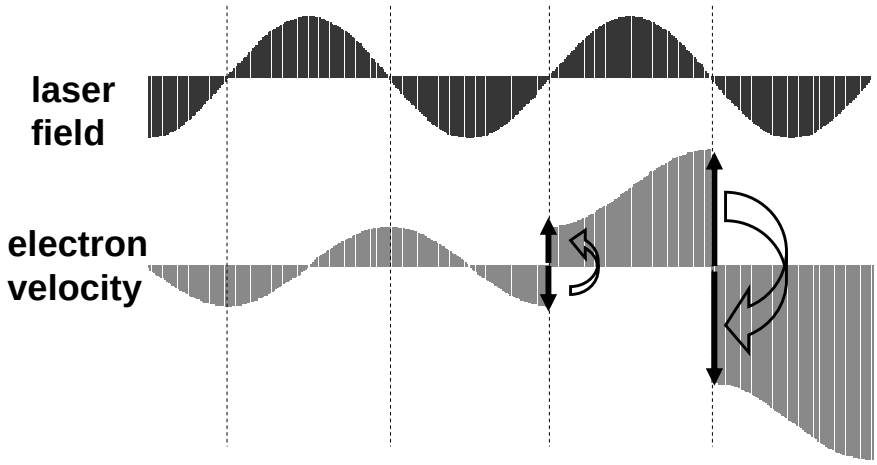

Figure 1.2: *Evolution of the velocity of an electron in a laser field. A free electron has no effective velocity gain beyond the quiver velocity. However, if the velocity of the electron is flipped periodically, the electron can monotonically increase its kinetic energy in the laser field.*

To test the efficiency of this heating mechanism and make quantitative estimates for the x-ray yields, we have developed a Monte Carlo simulation, which allows us to analyse the importance of different mechanisms for the heating of the cluster electrons. In the next chapter we will give an overview of the simulation method and some fundamental physical mechanisms like over-barrier ionization and x-ray production will be introduced. In the third chapter we will study the efficiency of elastic electron-ion scattering as a

heating mechanism for electrons in a laser field. For this we will switch off any competing heating mechanism. In the following chapters we will add physical features to the simulation of the cluster, making it more and more realistic. Each of the mechanisms introduced will be studied with respect to its influence on the electron heating. This procedure allows to distinguish the influence of the different mechanisms at play in the electron dynamics. Chapter four will introduce the charging and expansion of the cluster, as well as the subsequent monopole field acting inside and outside the cluster. The influence of the collective electron motion in the laser field which gives rise to a dipole field will be studied in chapter five. Chapter six will deal with the importance of electron-impact ionization of the cluster ions. Each of the models studied in this work will include some of these mechanisms. Table 1.1 gives an overview of the ingredients for each model. Finally, in chapter seven the parameter dependencies of the x-ray yield will be tested and the results compared to the experimental findings.

model	laser field	elastic electron-ion scattering	cluster charging and expansion	dipole field	electron-impact ionization
1	+	−	−	−	−
2	+	+	−	−	−
3	+	−	+	−	−
4	+	+	+	−	−
5	+	−	+	+	−
6	+	+	+	+	−
7	+	−	+	+	+
8	+	+	+	+	+

Table 1.1: *Overview of the processes included (+) and neglected (−) in each model.*

Chapter 2

The simulation: overview of the method and first ingredients

In the experiments [1, 2, 13] argon clusters with up to a mean number $N = 2.8 \cdot 10^5$ of atoms were produced. Charge states Ar^{q+} up to $q = 16$ were detected. This implies that up to $N_e = N \times q$ electrons and N ions have to be included in the simulation. As a molecular dynamics simulation with as many particles exceeds by far computer resources available today, we have opted for a Classical Trajectory Monte Carlo (CTMC) simulation with a mean field approach. Our Monte Carlo ensemble consists of N_{MTC} electrons that are scaled to the actual number of electrons N_e in the cluster by a scaling factor. The different physical mechanisms at play in the cluster will be introduced one by one in the next chapters. In the final version of the simulation, later referred to as model 8, the following elements will be included: After ionization from an atom or an ion at a time t_0, each electron is propagated classically. The equation of motion for the electron is solved using the velocity Verlet algorithm (see appendix B). The electron will experience not only the laser field, but also the mean field arising from the displacement of the electron distribution relative to the ionic background charge. Furthermore the electron can undergo elastic scattering at ionic cores and produce new electrons by electron impact ionization, which is also the mechanism which produces the inner-shell vacancies necessary for the emission of x-ray photons. Because of their large inertia, the motion of the cluster atoms (or ions) caused by the Coulomb explosion of the cluster happens on a much larger time scale than the movement of the electrons. We can therefore treat the cluster ions as a uniform spherical background charge, with a time dependent radius $R(t)$. Electron-ion scattering and electron impact ionization have then to be handled by a stochastic approach. To take into account interactions that depend on the total electron density distribution

$\rho_e(\vec{r}, t)$ a mean field is evaluated after each time step. These mechanisms will be explained in detail in the next chapters. However some fundamental ingredients of the simulation will already be introduced in this chapter: field ionization, which is the simplest mechanism to create the quasi-free electrons in the cluster, the equation of motion of the quasi-free electrons and the creation of x-ray photons, which allow to compare the model in its different stages to the experimental findings. Atomic units (see appendix A) are used throughout this work unless otherwise stated.

2.1 Field ionization

We refer to the ionization of the atoms (or ions) in the cluster as inner ionization, as opposed to outer ionization referring to charging of the cluster as quasi-free electrons leave the cluster. The inner ionization creates quasi-free electrons inside the cluster. We do not simulate the atomic structure of the cluster atoms and ions, therefore the simulation for a given electron begins with its ionization out of the atom or ion at the time t_0. Each time an inner ionization event occurs, the number of simulated electrons N_{MTC} increases by one. N_{MTC} is directly proportional to the number of quasi-free electrons in the cluster N_e. The average charge state q of the ions inside the cluster is determined by $q = \frac{N_e}{N}$. The two ionization mechanisms at play in the cluster are field ionization and electron impact ionization. Field ionization is responsible for the creation of the first quasi-free electrons. These electrons can then be accelerated and ionize more electrons by electron impact ionization. This mechanism will be treated in chapter 6. We focus in the following on field ionization.

The field inside the cluster tilts the atomic potential of the atoms, thus allowing electrons to escape from the atom (see fig. 2.1). Depending on the binding energy of the electron and the field strength, the electron can either tunnel through the potential barrier, or, if the field is strong enough, the electron can escape the atom by over-barrier ionization. The contribution from tunneling [17] can be neglected, as the time scale of a laser femtosecond pulse is too short to obtain a sufficient probability for tunneling: the field strength exceeds rapidly the threshold for over-barrier ionization. The threshold field strength F_{th} necessary for over-barrier ionization to take place, for an ion with charge state q and an ionization potential W_q, is given by the Bethe rule [18]:

$$F_{th} = \frac{W_q^2}{4(q+1)}. \tag{2.1}$$

For the first ionization ($q = 0$) of the atoms, the threshold field strength F_{th}

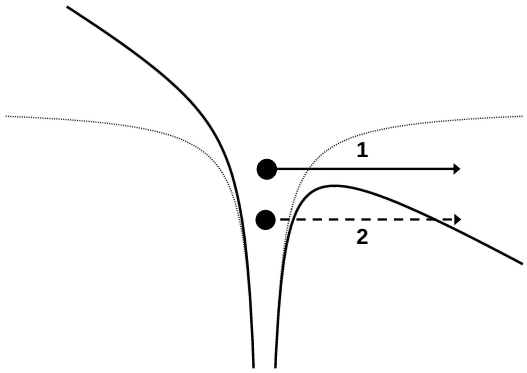

Figure 2.1: *Atomic potential (dotted curve) and atomic potential in constant electric field (solid line). The two ionization mechanisms that occur when the laser field acts on the atomic potential are schematically represented: 1: over-barrier ionization, 2: tunnel ionization*

must be reached by the laser field $F^L(t_0) = F_{th}$. At the time t_0 all the cluster atoms will be singly ionized and N quasi-free electrons will be created. The initial positions of the electrons are homogeneously distributed in the cluster and they are created with zero velocity. For further field ionization of the atoms, one has to take into account not only the laser field, but also the additional fields resulting from the charging of the cluster and the collective electron motion discussed in chapter 4 and 5. If one considers only the laser field and neglects additional fields, N quasi-free electrons will appear in the cluster each time the laser field is strong enough to ionize the cluster atoms (see fig.(2.2)). Table 2.1 lists the ionization potentials of different charge states of argon, together with the threshold fields for ionization and the laser intensities corresponding to these fields.

2.2 Evolution of electrons in the field

Once a quasi-free electron is created by inner ionization, it is propagated classically according to its equation of motion:

$$\ddot{\boldsymbol{x}} = -\boldsymbol{F}_L(t) - \boldsymbol{E}_{mean}(\boldsymbol{x}, t) + \boldsymbol{F}_{stoc}(\boldsymbol{x}, \dot{\boldsymbol{x}}, t). \tag{2.2}$$

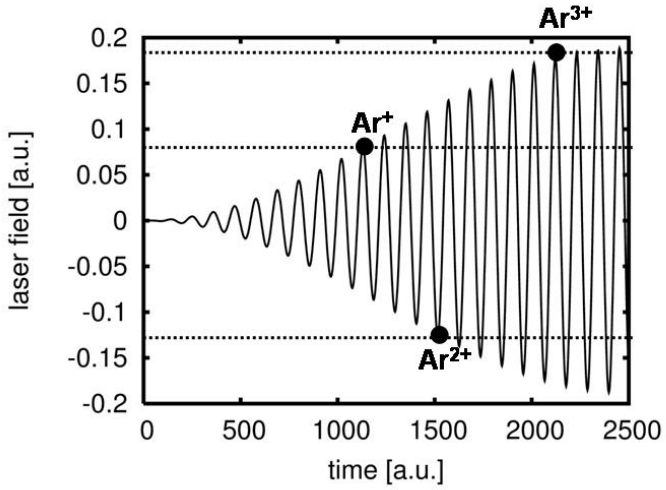

Figure 2.2: *First half of a laser pulse with* $I = 1.25 \cdot 10^{15}\mathrm{Wcm}^{-2}$ *and* $\tau = 60\mathrm{fs}$*(FWHM). The dashed lines represent the threshold field strengths necessary for the ionization of* Ar, Ar^+ *and* Ar^{2+} *(see table 2.1). The three points indicate the times when the laser field reaches these field strengths and* Ar^+, Ar^{2+} *and* Ar^{3+} *ions are created by over-barrier ionization.*

$\boldsymbol{F}_L(t)$ is the laser field. The laser pulse is of the length (FWHM) τ and is assumed to have the following shape:

$$\boldsymbol{F}_L(t) = \boldsymbol{F}_0 \sin^2(\frac{\pi t}{2\tau}). \tag{2.3}$$

For a linear polarization of the laser along the z-axis we have:

$$\boldsymbol{F}_0 = F_0^L \hat{\boldsymbol{z}} \sin(\omega t) \tag{2.4}$$

and for a circular polarization in the x-y plane we get:

$$\boldsymbol{F}_0 = F_0^C \hat{\boldsymbol{x}} \sin(\omega t) + F_0^C \hat{\boldsymbol{y}} \cos(\omega t). \tag{2.5}$$

For the energy of the circular and the polarized laser pulses to be equal, the following relation between the field strength for circular and linear polarization should hold:

$$F_0^C = \frac{F_0^L}{\sqrt{2}}. \tag{2.6}$$

The mean field $\boldsymbol{E}_{mean}(\boldsymbol{x}, t)$ depends on the relative position of the electrons to the ionic background charge. In the following it will be evaluated in different

q	W_q[a.u.]	F_{th} [a.u.]	I [10^{15}Wcm^{-2}]
0	0.58	0.08	0.25
1	1.01	0.13	0.58
2	1.50	0.19	1.22
3	2.20	0.30	3.20
4	2.76	0.38	5.10
5	3.35	0.47	7.65
6	4.57	0.75	19.5
7	5.28	0.87	26.6

Table 2.1: *Ionization potential W_q for Ar^{q+}, minimum field strength F_{th} for over-barrier ionization and corresponding laser intensity I.*

methods, the main idea being to split it in a monopole contribution treated in chapter 4 and a dipole contribution studied in chapter 5. $\boldsymbol{F}_{stoc}(\boldsymbol{x}, \dot{\boldsymbol{x}}, t)$ stands for the stochastic forces resulting from the elastic scattering at the ionic cores (see section 3.1) and from the electron impact ionization. As these forces depend also on the velocity of the particle, they may contribute to an effective damping force. As the electrons are treated as free particles evolving in a mean field and scattering stochastically, local fields, arising from the atomic structure of the cluster, are neglected. The influence of these local fields has still to be estimated. The equation of motion (2.2) is solved by the velocity Verlet algorithm which is described in more detail in appendix B. The step-size is chosen to be $\Delta t = 0.005\mathrm{fs} = 0.02\mathrm{a.u.}$ which has been checked to be sufficient to assure convergence.

2.3 X-ray production

Even though electron impact ionization will only be introduced in chapter 6, the production of K-shell vacancies, which are at the origin of the x-ray emission will already be included now. The production of inner-shell vacancies can be treated separately as the electrons in the inner shells make a negligible contribution to the electron impact ionization cross section due to their high binding energies. Indeed, the binding energy of the K-shell electrons of argon atoms is $E_K = 117\mathrm{a.u.}$ while the electrons in the $\mathrm{L_I}$-shell are bound with only $E_L \simeq 12\mathrm{a.u.}$. The probability that an electron with kinetic energy E_e produces a K-shell vacancy during the time interval Δt is determined by the total cross-section for this process $\sigma_K(E_e)$, the ionic target

density ρ and the distance Δx traveled by the electron during the time Δt:

$$P_K = \rho \sigma_K(E_e) \Delta x. \tag{2.7}$$

For each time step and each simulated electron this probability is determined. A random number x_{rnd} between 0 and 1 is generated and compared to P_K. If $x_{rnd} > P_K$ nothing happens. If $x_{rnd} < P_K$, a K-shell vacancy is produced, i.e. a new electron ($N_{MTC} \rightarrow N_{MTC} + 1$) is created at the position of the impact, and the kinetic energy of the impacting electron is reduced by E_K. The new electron is assumed to have zero velocity, as we are considering ionization processes near the threshold. The number N_K of these events is counted. We assume that the atom is instantaneously relaxed, and the inner vacancies are filled by electrons from the outer shells. The energy dependence of cross section for K-shell ionization $\sigma_K(E_e)$ is taken from experimental data [19]. Only the high energy tail of the electron energy distribution with E_e larger than the threshold for K-shell ionization can contribute. The number of K-shell vacancies N_K produced is directly related to the number N_X of x-ray photons produced by the fluorescence yield ω_f which depends on the charge state of the ions:

$$N_X = \omega_f N_K. \tag{2.8}$$

Chapter 3

Elastic electron-ion scattering

In this chapter we describe the implementation of elastic electron ion scattering in our simulation and show first encouraging results, which indicate that in a cluster-like environment elastic scattering at ionic cores can indeed enhance the heating of the electrons as described in the introduction.

3.1 Implementation in the simulation

Key ingredient of our simulation are the realistic differential cross sections for elastic scattering at singly, as well as multiply charged rare gas atoms. The cross sections are calculated by partial wave analysis [20] using parameterized Hartree-Fock potentials [21] for different ionic charge states. Figure (3.1) shows the differential elastic scattering cross section of Ar^{2+}. It indicates a significant probability for back scattering, for electron energies below 100a.u. ($\sim$ 2.7keV), which corresponds to several times the ponderomotive energy for laser intensities below $I = 10^{16}\mathrm{Wcm}^{-2}$. The minima for intermediate angles are referred to as Ramsauer-Townsend minima and are due to interference effects [22].

Argon clusters of sufficient size ($N \geq 1000$) have a face centered cubic (fcc) crystalline structure [23]. The nearest neighbour distance in the cluster is known to be 3.76Å and the atomic density in the cluster is $\rho = 2.66 \cdot 10^{22}\mathrm{cm}^{-3} = 3.94 \cdot 10^{-3}$a.u.. This solid state environment is included in the calculation of the scattering cross section by introducing a muffin-tin radius corresponding to half the initial mean inter-atomic distance in the cluster $R_{mt} = 3.5$a.u., however this correction has no significant influence on the large-angle scattering.

Similarly to the production of K-shell vacancies (see eq.(2.7)), the prob-

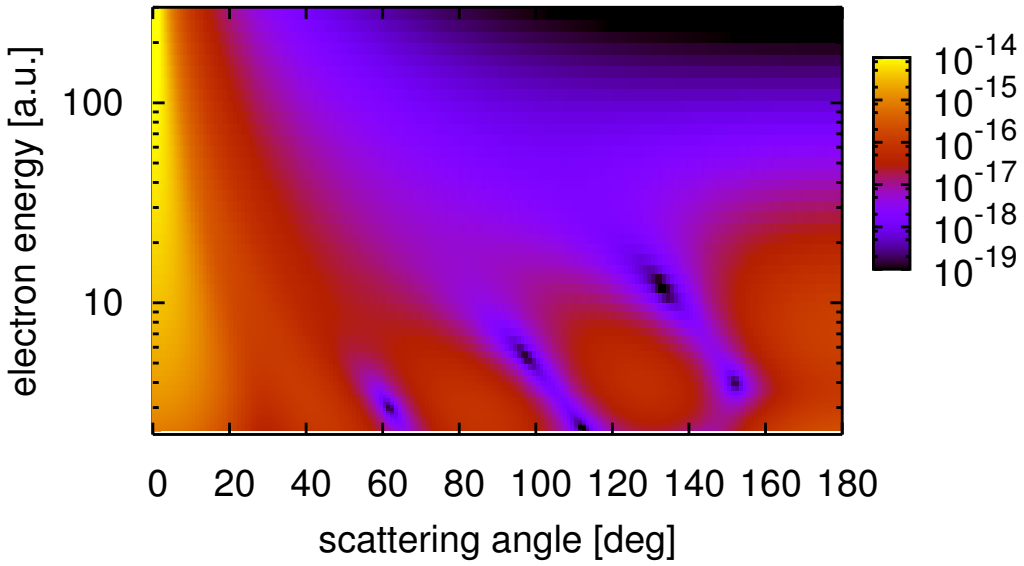

Figure 3.1: *Differential elastic scattering cross section (in a.u.) for* Ar^{2+}. *Note that the electrons energies as well as the cross sections are displayed on a logarithmic scale.*

ability for elastic scattering during the time interval Δt is given by:

$$P_{scatt} = \rho \sigma_{scatt} \Delta x. \tag{3.1}$$

The total elastic scattering cross section σ_{scatt} depends on the energy of the scattered electron and on the charge state q of the ion, for which the mean charge state of the ions in the cluster is taken. Again a random number is drawn, and if $x_{rnd} < P_{scatt}$, the electron is scattered. The scattering angle θ_{scatt} is determined by another random number according to the differential scattering cross section corresponding to the electron energy and the charge state of the ion. The velocity vector of the electron is redirected according to θ_{scatt} (see appendix C). Accordingly, the momentum just prior to the i^{th} collision $\boldsymbol{p}(t_i^-)$ is mapped onto the momentum after the elastic collision through

$$\boldsymbol{p}(t_i^+) = \boldsymbol{p}(t_i^-) + \Delta \boldsymbol{p}, \tag{3.2}$$

where $\Delta \boldsymbol{p}$ is the momentum transfer during core scattering. Backscattering ($\theta \simeq 180°$) corresponds to $\Delta \boldsymbol{p} = -2\boldsymbol{p}(t_i^-)$. This change of momentum can be

seen as the stochastic force $\boldsymbol{F}_{stoc}$ appearing in the equation of motion (2.2). However, the electron energy in the absence of the laser is conserved by these scattering events:

$$\frac{p(t_i^+)^2}{2} = \frac{p(t_i^-)^2}{2}. \tag{3.3}$$

3.2 Simulation results

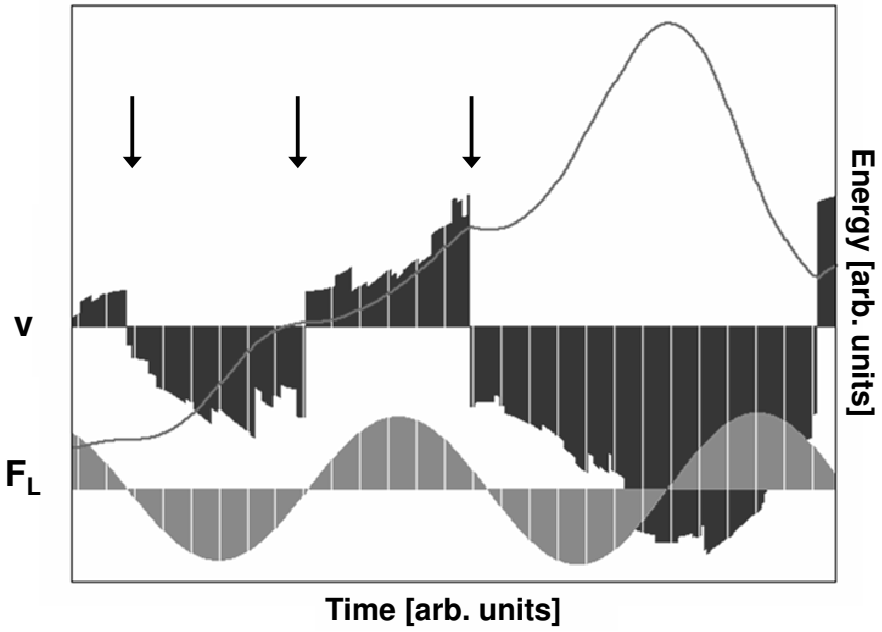

Figure 3.2: *The velocity component in field direction (upper black curve) and energy (line) of a single electron in a laser field are displayed. The jumps in the velocity are due to scattering events. Back scattering allows the electron to gain kinetic energy. The lower gray curve represents the laser field.*

In order to determine if the elastic scattering of electrons at cluster ions can indeed accelerate electrons in a laser field, we start by examining an electron in an infinitely large cluster (we therefore have no effects coming from the charging of the cluster) on which acts a (spatially uniform) laser field. The motion of the electron is assumed to be only influenced by the laser field and the elastic scattering at ions (model 2). The electrons thus

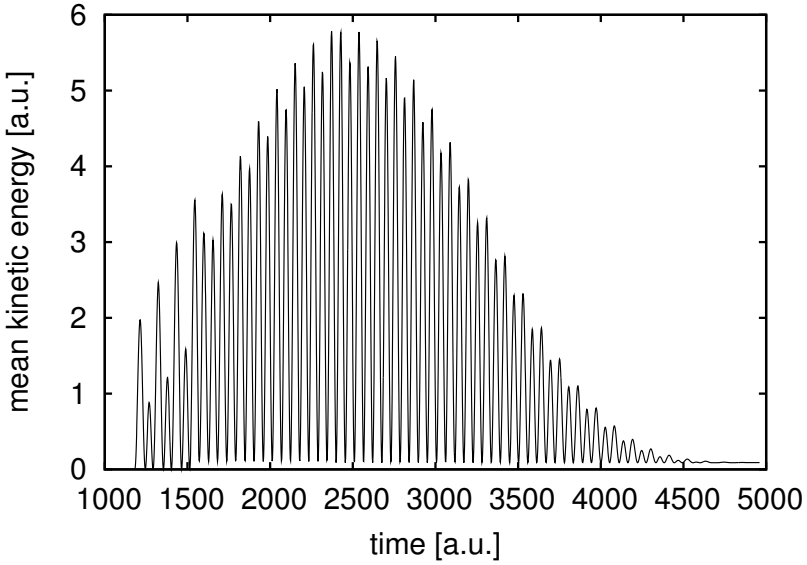

Figure 3.3: *Time evolution of the mean kinetic energy of electrons in an infinite cluster. The laser parameters were* $I = 1.25{\cdot}10^{15}\mathrm{Wcm}^{-2}$, $\lambda = 800nm$, $\tau = 60fs = 2500a.u.$. *Elastic scattering at ions was switched off (model 1).*

obey the following equation of motion:

$$\ddot{\boldsymbol{x}} = -\boldsymbol{F}_L + \boldsymbol{F}_{stoc}^{scatt}. \tag{3.4}$$

The laser field $\boldsymbol{F}_L(t)$ is assumed to have the simple form:

$$\boldsymbol{F}_L(t) = \hat{\boldsymbol{z}} F_0 \sin(\omega t) \sin^2(\frac{\pi t}{2\tau}). \tag{3.5}$$

The stochastic force $\boldsymbol{F}_{stoc}^{scatt}$ acts at discrete times and stands for the change of direction of the electron momentum when elastic scattering occurs. Figure 3.2 follows the evolution of the velocity and energy of one electron during two laser cycles closely mirroring the scenario depicted in figure 1.2. Whenever the electron scatters at an ion, the velocity is redistributed among the three velocity components. Thus the scattering events are marked by sudden jumps in the velocity in field direction. Forward scattering will produce only slight changes, while back scattering turns the velocity vector around. In this particular time interval, three back scattering events occur that allow the electron to gain additional energy. During the second laser cycle no back scattering occurs, and the electron looses again part of its energy.

Figures 3.3 and 3.4 study the time evolution of the mean kinetic energy $< E_e >$ of the electrons with respect to elastic scattering of electrons at

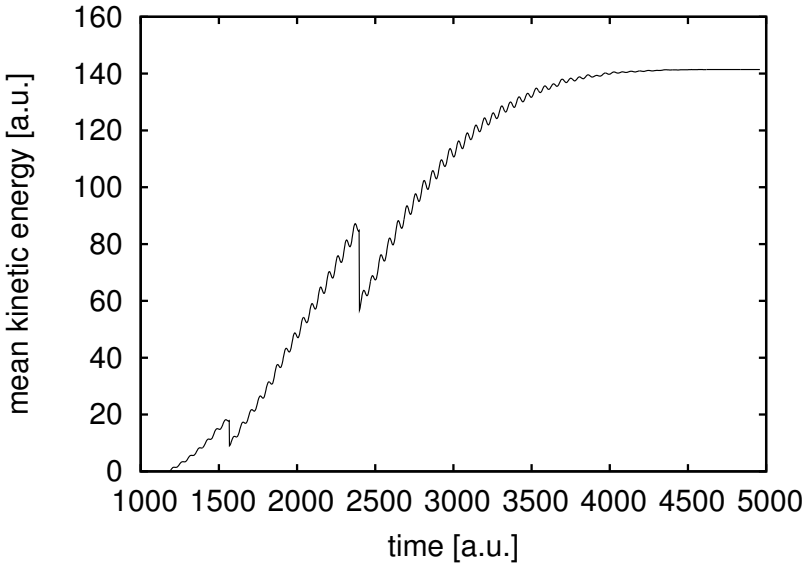

Figure 3.4: *Same as fig. 3.3, except for elastic scattering of the electrons at ions taken into account (model 2, eq.(3.4)). The two drops in the energy come from over-barrier ionization of the ions by the laser field supplying additional "cold" electrons.*

ions. If scattering is not taken into account (model 1, fig. 3.3), the electrons are only accelerated by the laser field. In this case the mean kinetic energy oscillates with twice the laser frequency, going back down to zero each time, as the electrons gain and lose their momentum during each half cycle of the laser (see fig. 1.2). The maxima of the energy oscillations follow the shape of the laser pulse. In a laser field $F(t) = F_0 \sin(\omega t)$, an electron can reach the maximum energy of $E_{max} = \frac{F_0^2}{2\omega^2}$. For an intensity of $I = 1.25 \cdot 10^{15}\mathrm{Wcm}^{-2}$, $E_{max} \simeq 5.5$a.u.. This indeed corresponds to the maximum energy reached by the electrons in the pulse. When taking into consideration elastic scattering (model 2, fig. 3.4), the energy $< E_e >$significantly exceeds the maximum energy the electrons would acquire by only oscillating in the field. The small oscillations with twice the laser frequency on top of the curve are due to the oscillatory motion in the field and are of the order of magnitude of the ponderomotive energy. The two drops in the energy are caused by the sequential over-barrier ionization of the ions. At these times the laser field reaches the threshold field for the production of Ar^{2+} and Ar^{3+} respectively, releasing N new electrons with zero kinetic energy in the cluster. In this infinite cluster all other accelerating or decelerating effects were neglected.

As a realistic cluster expands radially with time, one would expect that the heating mechanism described here loses of its efficiency toward the end of the pulse as the density of the ions, and thus the probability to scatter, decreases. This effect will be studied in the next chapter.

Chapter 4

Charging of the cluster

During their evolution, some of the quasi-free electrons will eventually reach the border of the cluster and leave the cluster. This is referred to as outer ionization and leads to a charging of the cluster. At each time step of the simulation, the number of electrons outside the cluster radius $R(t)$ is counted. The corresponding positive charge $Q(t)$ is the cluster charge. This charge gives rise to a radial expansion of the cluster resulting in the Coulomb explosion, as well as to an electric field inside and outside the cluster. This field is assumed to be radially symmetric, and can thus be seen as the monopole contribution to the mean field $\boldsymbol{E}_{mean}(\boldsymbol{x}, t)$ of equation (2.2).

4.1 Coulomb explosion of the cluster

We only consider a homogeneous radial expansion of the cluster. To obtain the time-dependent cluster radius $R(t)$, the equation of motion of an ion with charge q at the cluster surface is solved for a given cluster charge evolution $Q(t)$:

$$M\frac{\mathrm{d}^2R(t)}{\mathrm{d}t^2} = \frac{q(t)Q(t)}{R^2(t)} \tag{4.1}$$

M denotes the mass of the ion. $M = 7.3 \cdot 10^4$a.u.[25] for an argon ion. Due to the large inertia of the ions, the expansion takes place on the time scale of the laser pulse and not on the time scale of the electronic motion. For the charge q of the ion, the mean charge state of the ions $q = \frac{N_e}{N}$ is taken. This neglects the effect of the screening by the quasi-free electrons surrounding the ions. This could lead to a slower expansion of the cluster.

4.2 Monopole contribution to the mean field

To explore the radial charge distribution inside the cluster, we divide the cluster in 10 concentric spherical shells with a radial distance $\Delta R(t) = \frac{R(t)}{10}$. Further 10 shells divide the volume outside the cluster with $R(t) < r < 2R(t)$ to account for the screening of the cluster by the electrons that left the cluster. It has been tested that the simulation results stayed the same when using even more shells. At each time step the net charge $Q_i(t)$ of each shell is evaluated by counting the number of electrons and ions inside the shell. The total cluster charge $Q(t)$ can be evaluated by:

$$Q(t) = \sum_{i=1}^{10} Q_i(t) \tag{4.2}$$

The radial field corresponding to this charge distribution is given by:

$$E^{(0)}_{mean}(r,t) = \sum_{i=1}^{i_r-1} \frac{Q_i(t)}{r^2} + \frac{Q_{ir}(t)(r^3 - ((ir-1)\Delta R)^3)}{(ir\Delta R)^3 - ((ir-1)\Delta R)^3} \frac{1}{r^2} \tag{4.3}$$

Where $i_r = \left\lceil \frac{r}{\Delta R} \right\rceil$ is the index of the shell corresponding to the actual position r ($\lceil x \rceil$ denotes the closest integer larger than x). For $r > 2R(t)$, $E^{(0)}_{mean}(r,t) = \sum_{i=1}^{20} \frac{Q_i(t)}{r^2}$.

4.3 Simulation results

In the experiments the clusters are generated by a pulsed adiabatic expansion of a gaseous jet through a conical nozzle. The pressure before the nozzle is called the backing pressure P_0 and determines the mean number of atoms per cluster $\bar{N}$. Their relation for argon clusters is given by the following empirical expression [12]:

$$\bar{N} = 369.6 \cdot (P_0[\text{bar}])^{1.8} \tag{4.4}$$

We simulate a cluster with $N = 2.8 \cdot 10^5$ argon atoms, which corresponds to the mean cluster size in an experiment with a backing pressure $P = 40$bar. With a density of $\rho = 3.94 \cdot 10^{-3}$a.u. this leads to an initial radius of $R(0) = 258$a.u.. In addition to the laser field, the charging and expansion of the cluster is taken into account, while elastic electron-ion scattering is first neglected (model 3). The equation of motion of the electrons is now:

$$\ddot{\boldsymbol{x}} = -\boldsymbol{F}_L(t) - \boldsymbol{E}^{(0)}_{mean}(r,t). \tag{4.5}$$

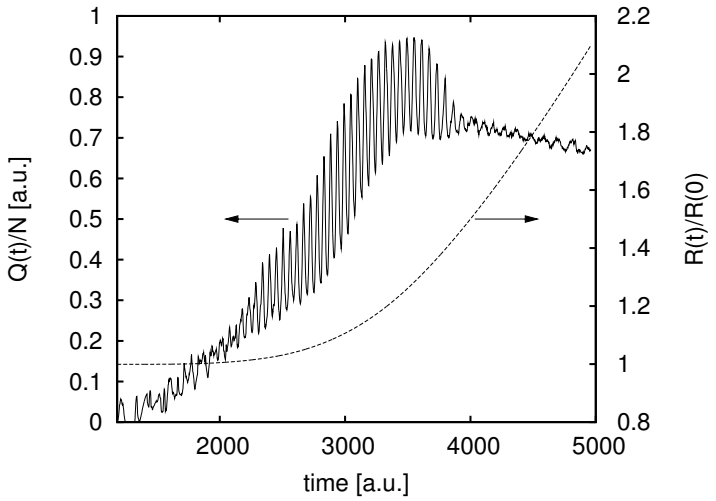

Figure 4.1: *Time evolution of the cluster charge per atom (left axis) and the ratio of cluster radius to initial radius (right axis). The cluster is subjected to the laser field, as well as charging and expansion (model 3, eq. (4.5)). The laser parameters were* $I = 1.25 \cdot 10^{15}\mathrm{Wcm}^{-2}$, $\lambda = 800nm$, $\tau = 60fs = 2500a.u.$.

The field $\boldsymbol{E}^{(0)}_{mean}(r,t)$ is given by equation (4.3).

Figure 4.1 shows the time evolution of the cluster charge $Q(t)$ per cluster atom N, and of the ratio of radius $R(t)$ and initial cluster radius $R(0)$. The cluster charge grows rapidly as soon as the first quasi-free electrons are produced by field ionization. As the laser is linearly polarized along the z-axis, the electrons in the vicinity of the cluster poles are driven periodically by the laser across the cluster border at the top and the bottom of the cluster, thus generating oscillations in the cluster charge with twice the laser frequency. Toward the end of the pulse, the cluster charge stops growing and even diminishes as the electrons have more difficulty overcoming the attractive field of the highly charged cluster. The cluster expansion sets in on a much slower time scale due to the large inertia of the cluster atoms. The main growth of the cluster is confined to the last quarter of the pulse, where it proceeds quickly, reaching twice the initial radius at the end of the pulse. The density ρ of the cluster ions has then dropped by a factor 8, making all stochastic processes like elastic electron-ion scattering or x-ray production much less probable.

The time evolution of the corresponding electrons' mean kinetic energy $< E_e >$ is displayed in figure 4.2. For the mean kinetic energy only the

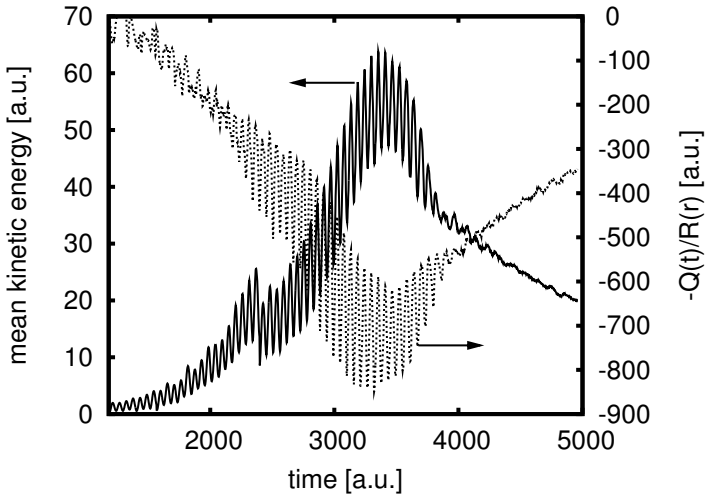

Figure 4.2: *Time evolution of the mean kinetic energy of the electrons in the cluster (solid line). The dashed line represents an estimation of the depth of the potential well inside the cluster. The cluster and laser parameters are the same as in figure 4.1. (model 3, eq. (4.5))*

electrons inside the cluster are taken into account, as it is the energy of these electrons that will influence the production of K-shell vacancies. When comparing $< E_e >$ to the the mean kinetic energy obtained for electrons only subjected to the laser field (figure 3.3), one notes that the charging contributes efficiently to the heating of the cluster electrons, resulting in a maximum of the mean kinetic energy at 60a.u., ten times higher than the maximum in figure 3.3. Even though the oscillations due to the periodic field are still pronounced, $< E_e >$ does not follow the shape of the laser pulse. The kinetic energy of the electrons reflects the virial theorem for the Coulomb potential inside the cluster. Its depth can be estimated by $-Q(t)/R(t)$, which is also displayed in figure 4.2 and corresponds very well to the shape of $< E_e >$. Initially the attractive potential grows rapidly due to the charging of the cluster. As the Coulomb explosion sets in and $R(t)$ rapidly increases, the internal potential stops growing and finally diminishes, just as the kinetic energy of the electrons. The build-up of the internal field due to the charging of the cluster is therefore an additional heating mechanism for the electrons.

Figures 4.3 and 4.4 repeat this simulation, only that they now include elastic electron-ion scattering (model 4). For this model, the equation of

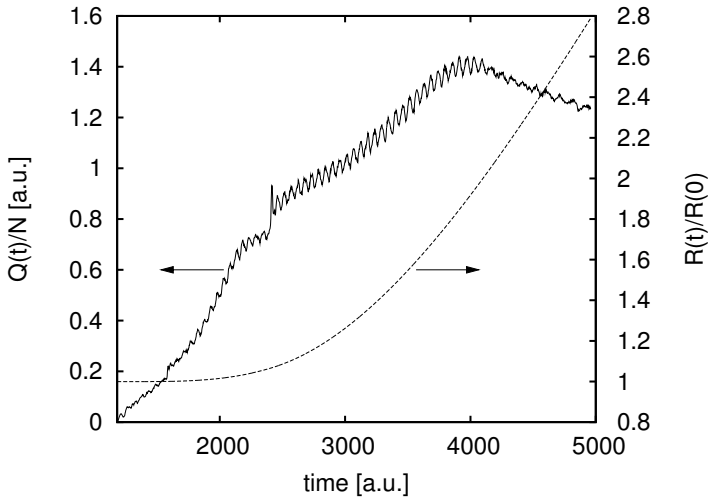

Figure 4.3: *Same as fig.4.1, but with elastic electron-ion scattering (model 4, eq. (4.6)).*

motion of the electrons is:

$$\ddot{\boldsymbol{x}} = -\boldsymbol{F}_L(t) - \boldsymbol{E}^{(0)}_{mean}(r,t) + \boldsymbol{F}^{scatt}_{stoc}. \tag{4.6}$$

It has been shown in the previous chapter that this mechanism is very efficient for heating electrons, and indeed, the energies reached now are nearly four times higher than the ones reached with cluster charging only. Moreover, the energy is nearly twice as high as the energy reached by elastic scattering alone, without taking into account outer ionization (model 2, figure 3.4). Figure 4.3 shows that the cluster charging takes place faster than for model 3 (fig. 4.1) reaching a 1.5 times higher cluster charge and resulting in a final radius that is equal to three times the initial one. As the mean kinetic energy is only weakly influenced by the laser oscillations, the two drops due to the two field ionization events become more pronounced. Again the evolution of $< E_e >$ is directly linked to the evolution of the potential well inside the cluster. Due to the elastic electron-ion scattering the electrons get heated up quickly after the first ionization burst, resulting in a faster growth of the cluster charge as the hot electrons reach the cluster border faster and have more energy to escape the attractive potential of the charged cluster. The heating by the charging of the cluster is thus enhanced by elastic scattering.

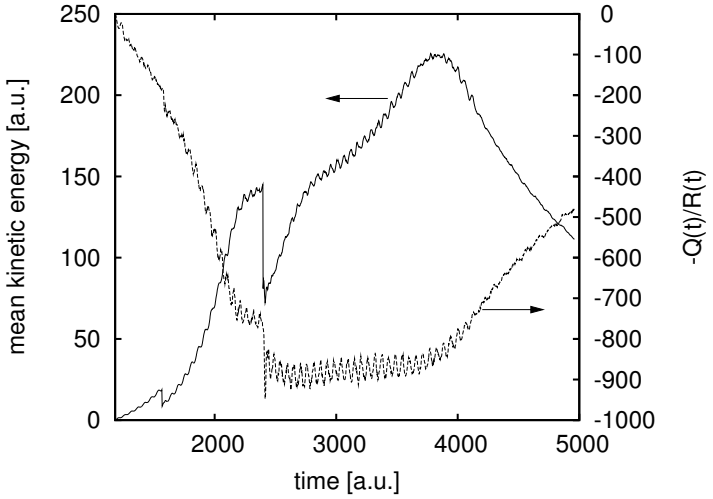

Figure 4.4: *Same as fig.4.2, but with elastic electron-ion scattering (model 4, eq. (4.6)).*

4.3.1 Study of the radial charge distribution

Figure 4.5 shows the time evolution of the radial charge distribution corresponding to the simulation including charging of the cluster and elastic electron-ion scattering. As previously explained, the simulation volume is divided radially into 20 equidistant shells, the ten inner shells modelling the cluster. The net charge $Q_i(t)$ of each of these shells is indicated corresponding to the color code. The dashed black line marks the cluster border. As the cluster expands with time, so does each of the shells. One observes that the cluster charge is mainly concentrated on the cluster surface. This seems reasonable as the fast electrons should screen the background charge in the center of the cluster better than on the surface. This result is confirmed by previous full simulations of the electron and ion dynamics [9]. One could therefore use a simplified model for the radial distribution in which the cluster charge $Q(t)$ is located on a spherical shell on the surface of the cluster.

The charge distribution $\rho_e^{(0)}(\boldsymbol{x}, t)$ depends on the radius R of the cluster and on the inner radius R_i of this shell (see fig.4.6).

$$\rho_e^{(0)}(\boldsymbol{x}, t) = \frac{Q(t)}{\frac{4\pi}{3}(R(t)^3 - R_i(t)^3)}[\Theta(r - R_i(t)) - \Theta(r - R(t))]. \qquad (4.7)$$

The charge is produced by unshielded cluster ions. The total charge of the

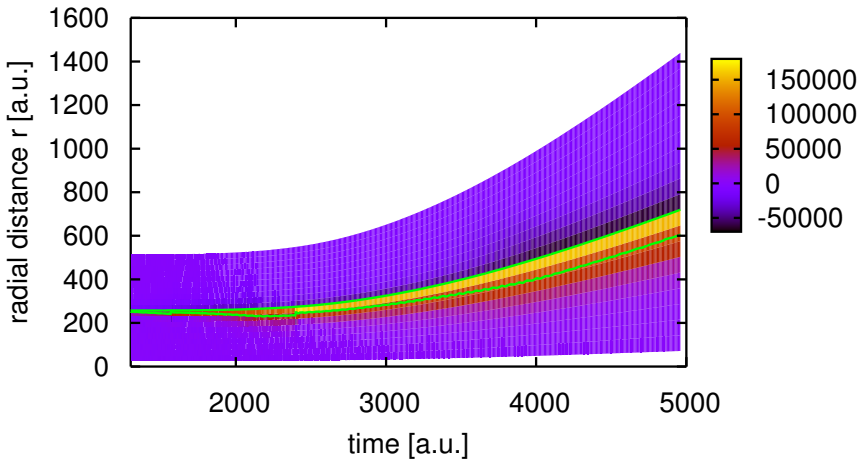

Figure 4.5: *Time evolution of the charge of the different shells dividing radially the simulation volume. The upper green line marks the cluster radius. As the cluster expands with time, so do the shells, always staying radially equidistant. The lower green line is the inner border R_i of the single shell containing the cluster charge when using the simplified model. The laser parameters are the same as in figure 4.1.*

ions in the shell must correspond to the total charge of the cluster:

$$\frac{4\pi}{3}(R(t)^3 - R_i(t)^3)\rho_{ion}(t)q(t) = Q(t). \tag{4.8}$$

The inner radius $R_i(t)$ therefore depends on the cluster charge $Q(t)$, the cluster radius $R(t)^3 = \frac{N}{4\pi/3\rho_{ion}(t)}$ and the mean charge state $q(t)$ of the ions:

$$R_i(t) = R(t)\sqrt[3]{1 - \frac{Q(t)}{Nq(t)}}. \tag{4.9}$$

The estimation of the inner radius $R_i(t)$ of the single shell is represented in figure 4.5 by the solid line and fits the actual radial charge distribution rather well. The radial electric field $E^{(0)}_{mean}(r,t)$ can now easily be calculated:

$$E^{(0)}_{mean}(r,t) = \begin{cases} 0 & r < R_i(t) \\ \frac{Q(t)}{R(t)^3 - R_i(t)^3}(r - \frac{R_i(t^3)}{r^2}) & R_i(t) < r < R(t) \\ \frac{Q(t)}{r^2} & R(t) < r. \end{cases} \tag{4.10}$$

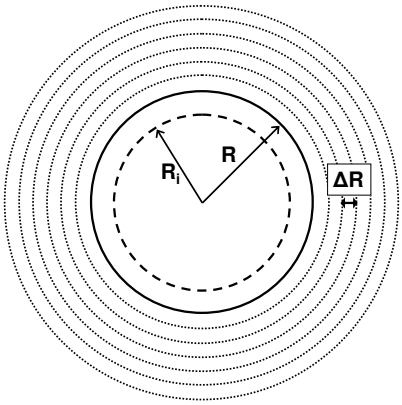

Figure 4.6: *The simplified surface-charge model for the radial charge distribution: the solid line represents the cluster boundary. The cluster charge is uniformly distributed between the inner dashed sphere and the cluster boundary. The outer spheres are equidistant with a distance of ΔR between them. They are used to determine the screening by the electrons outside of the cluster.*

To account for the screening of the cluster charge by the electrons that surround the cluster, one can divide the shell $R(t) < r < R(t) + R(0)$ into six spherical shells and count at each time step the number of electrons in each shell. The screening field is then evaluated just as in equation (4.3).

Figures 4.7 and 4.8 compare the results obtained with model 4 when using 20 shells and when using the surface-charge assumption. The results only differ slightly in the second half of the laser pulse. These results show that the assumption of the charge concentration on the cluster surface is justified in good approximation. This fact will be used in further theoretical considerations in the next chapter. However for simulations the more accurate model with 20 shells will be used.

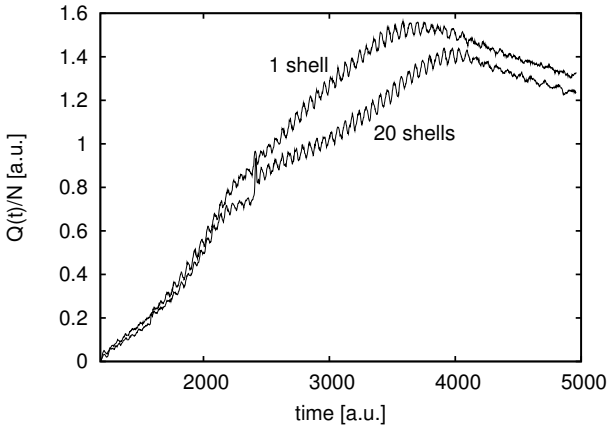

Figure 4.7: *Time evolution of the cluster charge per atom (left axis) calculated with the simplified surface-charge model (1 shell) and with 20 shells. The laser parameters are the same as in figure 4.1.*

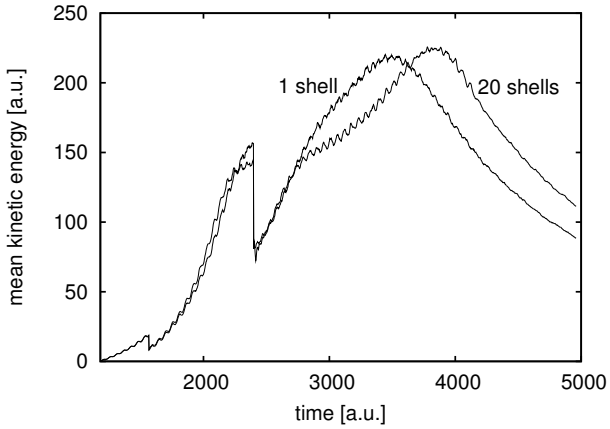

Figure 4.8: *Time evolution of the mean kinetic energy of the electrons in the cluster calculated with the simplified surface-charge model (1 shell) and with 20 shells. The laser parameters are the same as in figure 4.1.*

4.3.2 K-shell vacancies

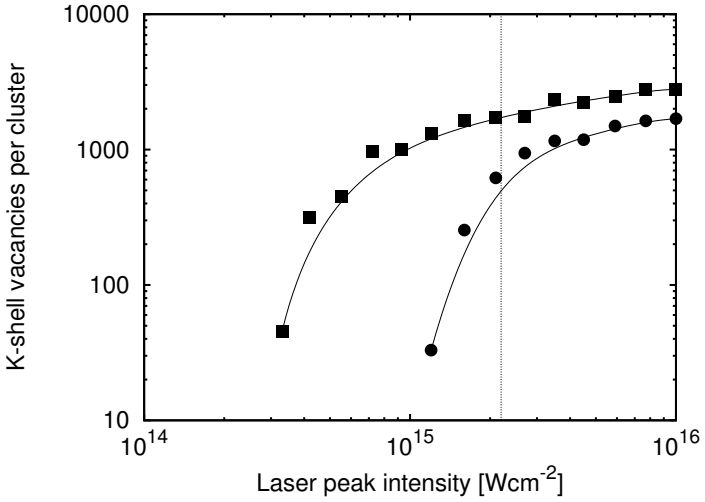

Figure 4.9: *Number of produced K-shell vacancies for different laser peak intensities. The results for the cases with (■, model 4, eq. (4.6)) elastic electron-ion scattering and without (●, model 3, eq. (4.5)) are compared (the solid lines are shown to guide the eye). The vertical dashed line marks the experimental intensity threshold for x-ray production. The size of the argon cluster was* $N = 2.8 \cdot 10^5$*. The laser duration was* $\tau = 60$fs*, the wavelength* $\lambda = 800$nm.

As the experimental findings are based on the measurement of the x-ray emission by the clusters, the simulation results for the produced K-shell vacancies are displayed in figure 4.9. Each point corresponds to the number of produced K-shell vacancies in a cluster with $N = 2.8 \cdot 10^5$ argon atoms irradiated by a laser pulse of length (FWHM) $\tau = 60$fs and wavelength $\lambda = 800$nm. Moreover the simulations have been conducted once with elastic electron-ion scattering (model 4, eq. (4.6), upper curve) and once without (model 3, eq. (4.5), lower curve). Once a certain laser peak intensity is reached, the number of produced vacancies increases quickly. This indicates the presence of an intensity threshold for the production of K-shell vacancies. Indeed, the heating mechanisms inside the cluster have to be efficient enough for the electrons to reach energies above the binding energy of the K-shell electrons, which is as high as $E_K = 117$a.u. for argon. The intensity threshold lies at about $I_{th} = 3 \cdot 10^{14}\mathrm{Wcm}^{-2}$ for the case with electron-ion scattering. For the case where scattering is neglected, the threshold is a factor 3 higher at approximately $I_{th} = 1 \cdot 10^{15}\mathrm{Wcm}^{-2}$. Above the threshold the number

of produced vacancies is rises quickly before reaching a saturation value in the order of magnitude of 2000 vacancies per cluster at $I = 1 \cdot 10^{16}\mathrm{Wcm}^{-2}$. At high intensities about 1.6 times more vacancies are produced when taking into account elastic electron-ion scattering. The lower threshold as well as the higher vacancy yield show that elastic electron-ion scattering is an efficient heating mechanism in clusters. The experimentally measured threshold is indicated by the vertical dashed line and lies at $I_{th} = 2.2 \cdot 10^{15}\mathrm{Wcm}^{-2}$, above the simulation results.

4.3.3 X-ray yield

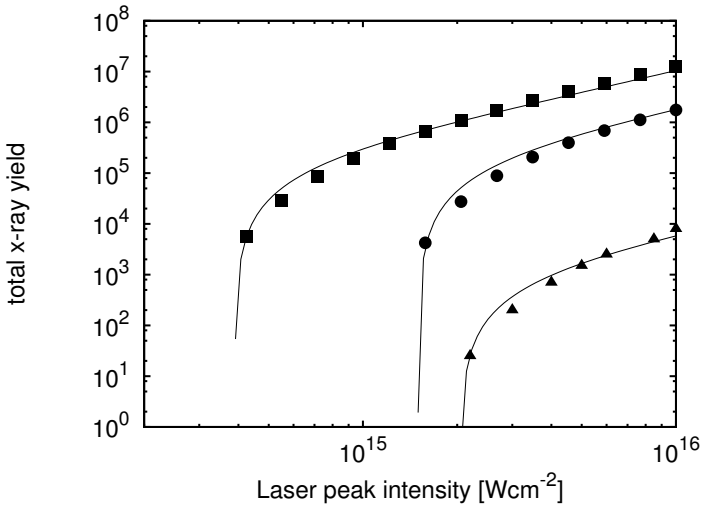

Figure 4.10: *Absolute x-ray yield for different laser peak intensities. The results for the cases with (■, model 4) elastic electron-ion scattering and without (●, model 3) are compared to the experimental results (▲). For each set of data, the solid line shows the evolution of the effective focal volume. For the case with scattering* $I_{th} = 3.9 \cdot 10^{14}\mathrm{Wcm}^{-2}$*, for the case without* $I_{th} = 1.5 \cdot 10^{15}\mathrm{Wcm}^{-2}$ *and for the experimental data* $I_{th} = 2.1 \cdot 10^{15}\mathrm{Wcm}^{-2}$*. The parameters are the same as in fig.4.9.*

To allow a first quantitative comparison with the experimental data, one has to convert the number of K-shell vacancies per cluster into the absolute x-ray yield measured in the experiments.

The number of K-shell vacancies N_K is related to the number of emitted x-rays N_X by the fluorescence yield ω_f:

$$N_X = \omega_f N_K \tag{4.11}$$

For neutral argon the fluorescence yield is $\omega_f \simeq 0.11$, which is still valid in good approximation when the charge state of the ions is around $q = 4$.

Furthermore the experiment can not be performed on a single cluster, but many clusters are irradiated by the laser pulse within the measurement volume. Moreover, the peak intensity of the laser pulse is not equal in the whole volume, i.e. the clusters experience different laser intensities I_0 depending on their position. The spatial pulse intensity profile is gaussian to a good degree of approximation:

$$I(r,t) = I_0 \exp\left(-\frac{2r^2}{w_0^2}\right). \tag{4.12}$$

That implies that to calculate the absolute x-ray yield for a given peak intensity I_0 (corresponding to one point in the fig. 1.1) one has to simulate an ensemble of clusters at laser peak intensities reaching from the threshold for K-shell vacancy production up to I_0. The results of these simulations is displayed in figure 4.9. The number of clusters experiencing a certain peak intensity depends on the volume where the laser has this intensity. The volume $V(I)$ which is the volume where the laser intensity lies between I and I_0 is given by [12]:

$$V(I) = \pi z_R w_0^2 \left\{ \frac{2}{9}\left(\frac{I_0}{I} - 1\right)^{3/2} + \frac{4}{3}\left(\frac{I_0}{I} - 1\right)^{1/2} - \frac{4}{3}\arctan\left[\left(\frac{I_0}{I} - 1\right)^{1/2}\right] \right\} \tag{4.13}$$

where z_R is the Rayleigh length and is equal to $z_R = 0.95$mm in the experiment. The beam waist w_0 is taken as the radius at $1/e^2$ and is approximately $w_0 = 15.55\mu$m [12]. By taking the difference of $V(I_1)$ and $V(I_2)$ one can therefore calculate the volume where the laser peak intensity lies between I_1 and I_2. The density of clusters in the measurement volume depends on the backing pressure P used in the experiment:

$$\rho_{cl}[\mathrm{cm}^{-3}] = 4.172 \cdot 10^{13} \frac{P_0[\mathrm{bar}]}{\bar{N}} \tag{4.14}$$

Figure 4.10 shows the simulation results for the total x-ray yield and compares it with the experimental data. The simulation data as well as the experimental data follow the evolution of the effective focal volume which is represented as a solid curve for each of the data sets. The effective focal volume $V(I_{th})$ is the volume in which the laser peak intensity exceeds a certain threshold I_{th} which is determined by fitting the data and which can be seen as an estimate for the threshold for x-ray production. For large laser intensities the effective focal volume follows a $I^{3/2}$ law (see eq.(4.13) which

can also be seen in the simulation and the experiments. However, the yields obtained from the simulations are much higher than the experimental ones. This indicates that the cluster charging and the elastic electron-ion scattering are both very efficient heating mechanisms. To achieve a good quantitative agreement with the experiments it is, however, necessary to include further mechanisms in the simulation.

Chapter 5

Polarization of the cluster

As discussed in the previous chapter, when only considering the monopole contribution of the mean field $\boldsymbol{E}^{(0)}_{mean}(r,t)$ arising from the charging of the cluster, most of the inside of the cluster ($r \lesssim R_i(t)$) is shielded and only the laser field is present. However, one expects that the laser field causes a polarization of the cluster, by forcing the electrons into an oscillatory motion along the polarization axis of the laser, thus generating a dipole contribution $\boldsymbol{E}^{(1)}_{mean}(r,\theta,t)$ to the mean field. This additional field inside the cluster will not only have an influence on the dynamics of the quasi-free electrons, but also on the over-barrier ionization, for which one now has to consider the combined field of laser and polarization.

5.1 The $r-\theta$ grid

To study these effects, one needs to include not only the radial charge distribution, but also the distribution with respect to the angle θ enclosed with the polarization direction of the laser (i.e. the z-axis for a linearly polarized laser). To do this, one divides the cluster and its surroundings into a $r-\theta$ grid. Each cell is a volume section of the cluster that is rotationally symmetric around the z-axis. For reason of statistics we chose a grid where the cells have all equal volume as shown in figure 5.1. After each time step the net charge in each of these cells is evaluated by counting the number of electrons and ions. For this discrete charge distribution one then has to solve the discretized Poisson equation to get the potential which determines the mean field $\boldsymbol{E}_{mean}(r,\theta,t)$. The mathematical details of the discretization are given in appendix D. The boundary condition for large r is determined by the requirement that far away from the cluster the potential is governed by

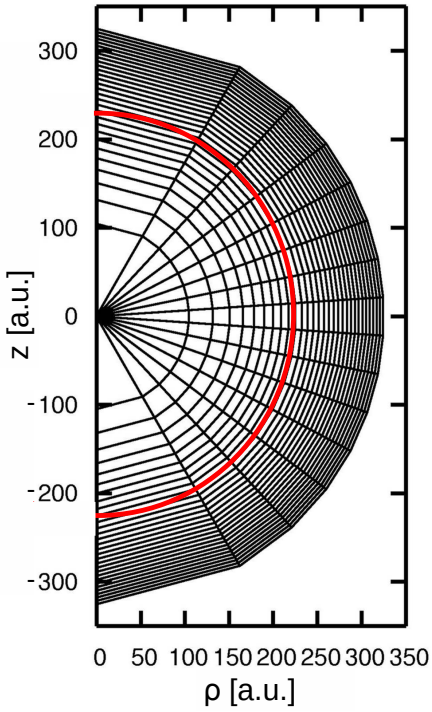

Figure 5.1: *$r-\theta$ discretization of the simulation volume. The red line marks the cluster boundary. Each cell represents a volume obtained when rotating the section about the z-axis. These cells are constructed to have equal volume.*

the screened space charge Q_{far} and the dipole moment in z-direction p_z:

$$\phi(r,\theta,t) = \frac{Q_{far}(t)}{r} + \frac{p_z \cos(\theta)}{r^2} \qquad \text{for large r.} \tag{5.1}$$

Q_{far} and p_z can both be calculated by integration the charge distribution $\rho_e(r,\theta,t)$ over the whole simulation volume V:

$$Q_{far} = \int_V \rho_e(r,\theta,t)\mathrm{d}^3\mathrm{r} \tag{5.2}$$

$$p_z = \int_V r\cos(\theta)\rho_e(r,\theta,t)\mathrm{d}^3\mathrm{r}. \tag{5.3}$$

The cluster charge $Q(t)$ can be calculated similarly

$$Q(t) = 2\pi \int_0^{R(t)} \mathrm{dr} \int_0^{\pi} \mathrm{d}\theta \rho_e(r, \theta, t). \tag{5.4}$$

To avoid problems with the discretization around the cluster boundary, the grid expands together with the cluster to ensure that the cluster boundary always lies on a grid line.

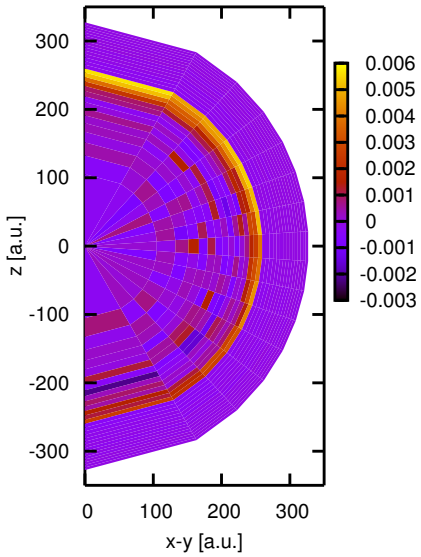

Figure 5.2: *$r - \theta$ distribution of the charge density at the time $t = 1905$a.u.. The cluster border is easily identifiable as the border between the positive (yellow, red) and outer negative (purple) charge regions. The laser parameters are $I = 1.25 \cdot 10^{15}\mathrm{Wcm}^{-2}$, $\lambda = 800nm$, $\tau = 60fs = 2500a.u.$.*

We now simulate the same cluster as in the previous chapter, i.e. $N = 2.8 \cdot 10^5$ argon atoms and a laser intensity of $I = 1.25 \cdot 10^{15}\mathrm{Wcm}^{-2}$ with a duration of $\tau = 60\mathrm{fs} \simeq 2500$a.u., linearly polarized along the z axis. However we now solve the Poisson equation on the $r - \theta$ grid at each time step. Furthermore elastic electron-ion scattering is included. The simulation volume is divided into a 30×15 $r - \theta$ grid, where the first 15 r steps divide the cluster (see fig.5.1). Figure 5.2 shows the charge distribution at the time

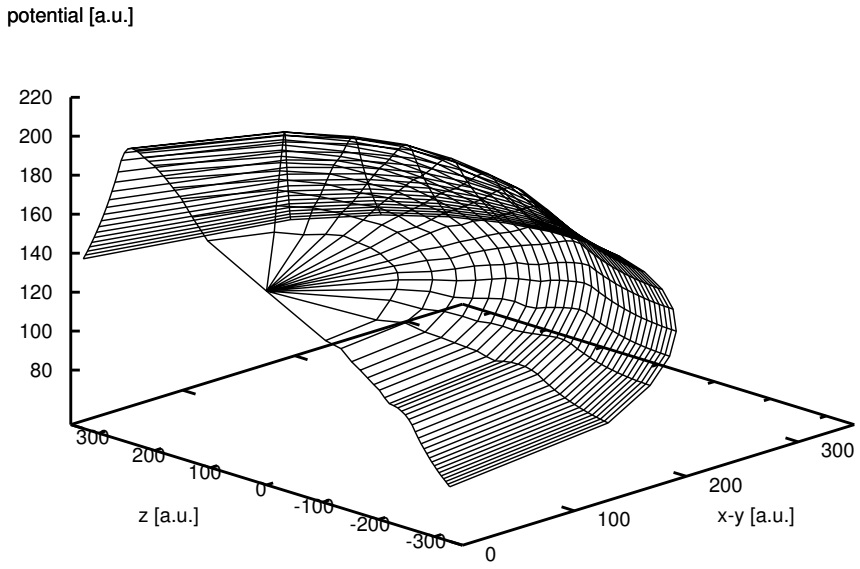

Figure 5.3: *$r-\theta$ dependence of the potential. The potential has been calculated from the charge distribution shown in fig. 5.2.*

$t = 1905$a.u.. Again the cluster charge is concentrated at the cluster surface, but a inhomogeneous distribution with respect to the θ angle can be observed, more charge being concentrated at the upper pole of the cluster than on the lower pole. This θ dependence of charge distribution arises from the polarizing effect of the laser which shifts the whole electron cloud along its polarization axis (the z axis). However it is still clearly visible that the inner of the cluster is in mean well shielded by the quasi-free electrons. The potential calculated from this charge distribution by solving the Poisson equation is depicted in figure 5.3. The potential has the morphology of a typical well potential one would expect for a charged sphere with its charge concentrated on the surface. However the bottom of the well is homogeneously tilted due to the dipole moment.

This simulation was run with one simulated electron representing 9 equivalent electrons ($N_e/N_{MTC} = 9$). Nevertheless, figure 5.2 displays statistical fluctuations of the charge density inside the cluster which give rise to fluctuations in the potential that can cause instabilities in the equation of motion of the electrons. This fluctuations are understandable as the inside of the

cluster is divided into 225 cells, which amounts to a ratio of 138 electrons per cell after the first ionization burst. This ratio gets worse as the electrons begin to leave the cluster. Moreover the time evolution of the cluster charge and the mean electron energy are not yet stable with respect to the number of cells in the grid, indicating that more cells are necessary. Simulations have shown that at least a 30×30 grid inside the cluster is needed. Of course the problems of the cluster statistics then get even more severe. That is the reason why we opted for a simplified model that takes into account dipole and monopole contribution to the potential without calculating the exact potential at each time step.

5.2 Simplified model for the dipole field

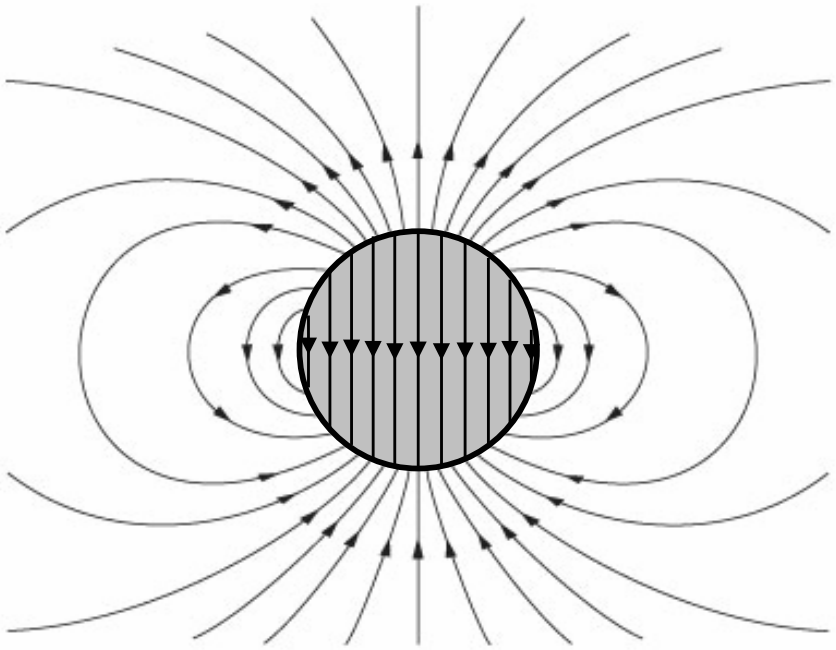

Figure 5.4: *Electric field inside and outside of a polarized sphere.*

The rather simple morphology of the potential calculated by solving the Poisson equation (fig. 5.3) encourages the idea of building a simpler model which treats the monopole and dipole contribution to the field separately. The modeling of the charging of the cluster has already been discussed in

the previous chapter and therefore we use for the monopole contribution to the field simply the radial field $\boldsymbol{E}^{(0)}_{mean}(r,t)$ defined in equation ((4.3)). To include the polarization effects of the cluster, one can make use of the simple model of the polarized sphere [26]. The dipole moment is assumed to be due to the small displacement of a sphere of uniform negative charge against a sphere of equal uniform positive charge. The electric field inside the sphere is then uniform and oriented in the opposite direction of the dipole moment:

$$\boldsymbol{E}^{(1)}_{mean}(t) = -\frac{\boldsymbol{p}(t)}{R(t)^3} \qquad \text{for } r < R(t) \tag{5.5}$$

The external electric field is that of a central dipole $\boldsymbol{p}(t)$:

$$\boldsymbol{E}^{(1)}_{mean}(t) = \frac{2\boldsymbol{p}(t)\cos(\theta)}{r^3}\hat{\boldsymbol{e}}_r + \frac{\boldsymbol{p}(t)\sin(\theta)}{r^3}\hat{\boldsymbol{e}}_\theta \qquad \text{for } r > R(t) \tag{5.6}$$

As shown in figure 5.4, the dipole field $\boldsymbol{E}^{(1)}_{mean}(t)$ is discontinuous at the cluster surface, and even changes sign at the poles of the cluster.

The dipole moment $\boldsymbol{p}(t)$ depends on the positions $\boldsymbol{x}_i$ of the electrons and the positions $\boldsymbol{x}^{(0)}_i$ of the corresponding ions, i.e. the position where the electrons were created:

$$\boldsymbol{p}(t) = \frac{N_e}{N_{MTC}} \sum_{i=1}^{N_{MTC}} (-\boldsymbol{x}_i + \boldsymbol{x}^{(0)}_i) \tag{5.7}$$

As the electrons that left the cluster, have a negligible influence on the dynamics inside the cluster, the sum in equation (5.7) is restricted to the electrons that fulfill $r < 1.3R(t)$.

The dipole moment of the cluster is dominated by the electron dynamics inside the cluster as the positive ions are distributed homogeneously in the spherical cluster. Therefore $\boldsymbol{p}(t) \approx -\sum_i^{N_e} \boldsymbol{x}_i(t)$. In a laser field $\boldsymbol{F}_L = \boldsymbol{F}_0 \sin\omega t$, the time evolution of the dipole moment can therefore be studied by examining the following differential equation:

$$\ddot{\boldsymbol{p}}(t) + \frac{N_e}{R^3}\boldsymbol{p}(t) = N_e\boldsymbol{F}_0 \sin(\omega t) \tag{5.8}$$

This is the equation for a driven harmonic oscillator with eigenfrequency $\omega_p^2 = \frac{N_e}{R^3}$. The amplitude of the oscillation is given by:

$$\boldsymbol{A}_p = \frac{N_e\boldsymbol{F}_0}{\omega_p^2 - \omega^2} \tag{5.9}$$

With $\omega^2 = 0.057^2$a.u. $\simeq 0.003$a.u. and $\omega_p^2 \sim 2.8 \cdot 10^5/250^3$a.u. $\simeq 0.018$a.u. we have $\omega_p^2 > \omega^2$. The oscillation of the dipole moment is therefore in phase

with the laser field. This produces an electric field inside the cluster that is oriented against the laser field, and therefore reduces the total electric field inside the cluster. The effective field inside the cluster can be estimated as:

$$\boldsymbol{E}_{eff}(t) = \boldsymbol{F}_L(t) + \boldsymbol{E}_p(t) = \boldsymbol{F}_0 \left(1 - \frac{\omega_p^2}{\omega_p^2 - \omega^2}\right) \sin(\omega t) \tag{5.10}$$

The larger ω_p becomes, i.e. the more electrons the cluster contains, the smaller will be the effective field inside the cluster. This simple estimation of the dipole moment does neither take into the additional internal fields arising at the border of the cluster due to the charging of the cluster, nor the effect of elastic electron-ion scattering. These effects can result in a phase shift between the dipole moment and the laser, thus enhancing the internal effective field. Furthermore dissipative effects like inelastic scattering at electrons can damp the oscillation. This can also create a phase shift between the dipole moment and the laser field. However in these cases the additional acceleration due to the large effective field will be counteracted by the loss of energy due to the damping.

5.3 Simulation results

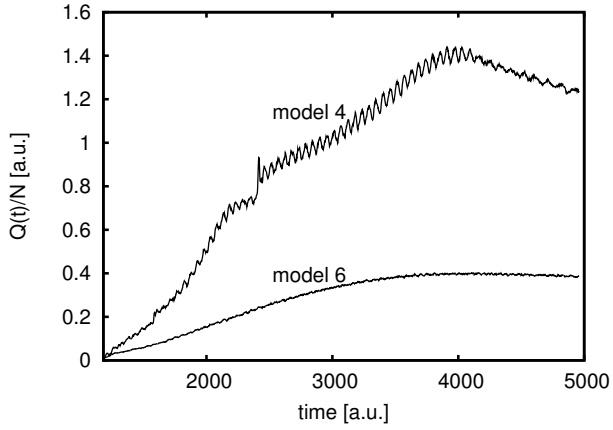

Figure 5.5: *Time evolution of the cluster charge per atom. The model now includes elastic scattering at ionic cores, as well as the monopole and the dipole field (lower curve, model 6). The result is compared with the case of the previous chapter where the dipole field is neglected (upper curve, model 4). The laser parameters are* $I = 1.25 \cdot 10^{15}\mathrm{Wcm}^{-2}$, $\lambda = 800nm$, $\tau = 60fs = 2500a.u.$.

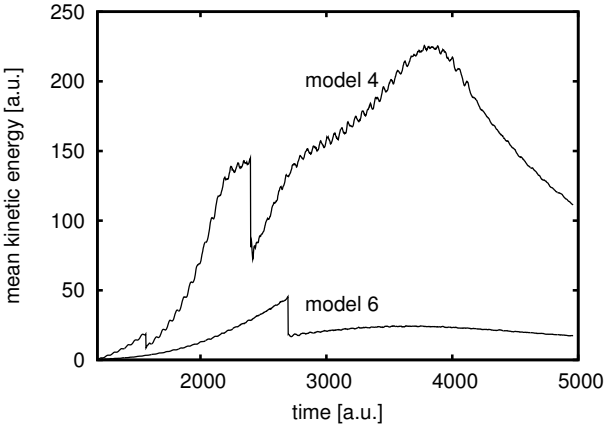

Figure 5.6: *Time evolution of the mean kinetic energy of the electrons in the cluster. The model includes elastic scattering at ionic cores, as well as the monopole and the dipole field (lower curve, model 6). The result is compared with the case of the previous chapter where the dipole field is neglected (upper curve, model 4). The drops in the mean energy are due to ionization events. The laser parameters are the same as in fig. 5.5.*

We now simulate the same cluster as in section 5.1 ($N = 2.8 \cdot 10^5$ argon atoms, $I = 1.25 \cdot 10^{15}\mathrm{Wcm}^{-2}$, $\tau = 60\mathrm{fs} \simeq 2500\mathrm{a.u.}$). The monopole contribution to the field is evaluated as described in the previous chapter by dividing the simulation volume in 20 radially equidistant shells, of which 10 lie inside the cluster. Moreover the model of the polarized sphere presented in the previous section is used to incorporate polarization effects in the simulation. Elastic electron-ion scattering is also included (model 6). In this model the electrons obey the following equation of motion:

$$\ddot{\boldsymbol{x}} = -\boldsymbol{F}_L(t) - \boldsymbol{E}^{(0)}_{mean}(r,t) - \boldsymbol{E}^{(1)}_{mean}(\boldsymbol{r},t) + \boldsymbol{F}^{scatt}_{stoc}. \tag{5.11}$$

Figure 5.5 shows the time evolution of the cluster charge and compares it to the case without the dipole contribution (model 4, eq. (4.6)). Due to the polarization effects the charging of the cluster is much slower and the maximum charge reached is less than half the one without dipole field. The mean kinetic energy of the electrons (fig. 5.6) is reduced. This is not surprising, as equation (5.8) implies that the field inside the cluster produced by the dipole moment is directed against the laser field, thus slowing down the motion of the electrons. This is demonstrated in figure 5.7 giving the effective field acting inside the cluster, i.e. the sum of laser field and dipole field. The monopole field can be neglected due to the shielding of the inside

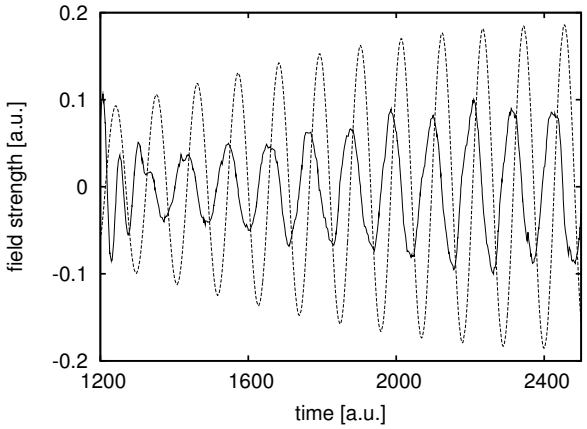

Figure 5.7: *Time evolution of the electric field acting inside the cluster (solid line). This field is the sum of the laser field and the dipole field. The laser field is also shown (dashed line). The laser parameters are the same as in figure 5.5.*

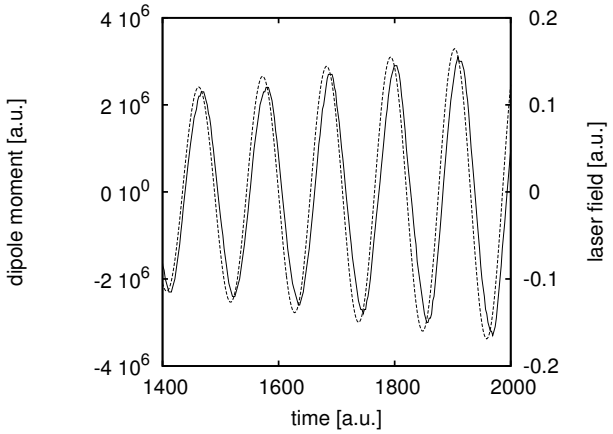

Figure 5.8: *Time evolution of the dipole moment (solid line). To study the phase shift the laser field is also shown (dashed line, right axis). The laser parameters are the same as in figure 5.5.*

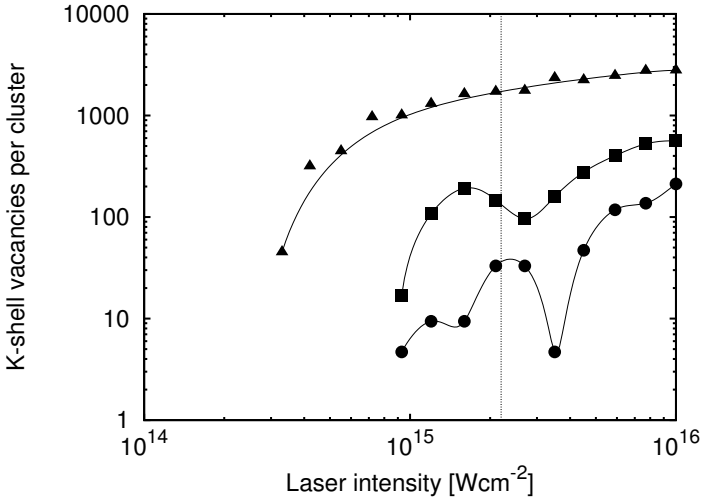

Figure 5.9: *Number of produced K-shell vacancies for different laser peak intensities. The results for the cases with elastic electron-ion scattering but without dipole field (▲, model 4), with elastic electron-ion scattering and with dipole field (■, model 6) and without electron-ion scattering but with dipole field (●, model 5) are compared (the solid lines are shown to guide the eye). The vertical dashed line marks the experimental intensity threshold for x-ray production. The size of the argon cluster was* $N = 2.8 \cdot 10^5$. *The laser duration was* $\tau = 60$fs, *the wavelength* $\lambda = 800$nm.

of the cluster. Indeed the effective field is smaller than the laser field. This also explains why the ions get only ionized twice and not three times as in the case without dipole contribution. The ionization events can be deduced from the drops in the mean energy. Already after the first laser cycle the phase of the dipole moment (fig. 5.8) is slightly shifted with respect to the laser field. This phase shift can be due to the charging of the cluster and the subsequently arrising additional fields inside the cluster and due to the elastic electron-ion scattering which scatters the electrons off the polarization axis.

5.3.1 K-shell vacancies

As in section 4.3.2, the number of produced K-shell vacancies with different models is examined in figure 5.9. For comparison the results of the previous chapter with elastic electron-ion scattering but without polarization effects (upper curve, model 4) is shown. The two lower curves give the results when

the dipole field is considered in the model. The middle curve corresponds to the case where elastic electron-ion scattering was included (model 6), for the lowest curve it was neglected (model 5). When including polarization effects the intensity threshold for the production of K-shell vacancies lies at about $I_{th} = 9 \cdot 10^{14}\mathrm{Wcm}^{-2}$. When taking into consideration the elastic electron-ion scattering, the number of produced vacancies is by a factor 5 lower than in the case without the dipole field, but is more than a factor 2 higher than without scattering. One also notes that contrary to the previous results, the number of vacancies does not grow monotonically with the laser intensity any more. This is due to the fact that, apart from the elastic scattering, no damping mechanisms are present in the cluster. Therefore the transient states can be rather long, leading to effective fields inside the cluster that depend strongly on the ionization times and that are not necessarily smaller than the laser field. As the elastic electron-ion scattering deflects the electrons from the polarization axis it is a damping mechanism and therefore accelerates the transition to a steady state as in figure 5.7 where the effective field is smaller than the laser field and has the same frequency. This explains why the irregularities in the dependence from the laser intensity are more pronounced in the case without elastic electron-ion scattering.

5.3.2 X-ray yield

As discussed in section 4.3.3, the absolute x-ray yield can be calculated from the number of K-shell vacancies per cluster. The results are displayed in figure 5.10. The irregularities of the yield per cluster have been averaged out by the intensity distribution in the simulation volume and the absolute yield grows monotonically following the evolution of the effective focal volume. The yields are closer to the experimental data than without dipole field but still more than an order of magnitude larger. Moreover the intensity threshold is still a factor 2 lower than the experimental one. Another problem with the present model is that the charge states of the argon ions inside the cluster at intensities near the threshold are not much higher than $q = 4$. However in the experiments much higher charged ions were detected.

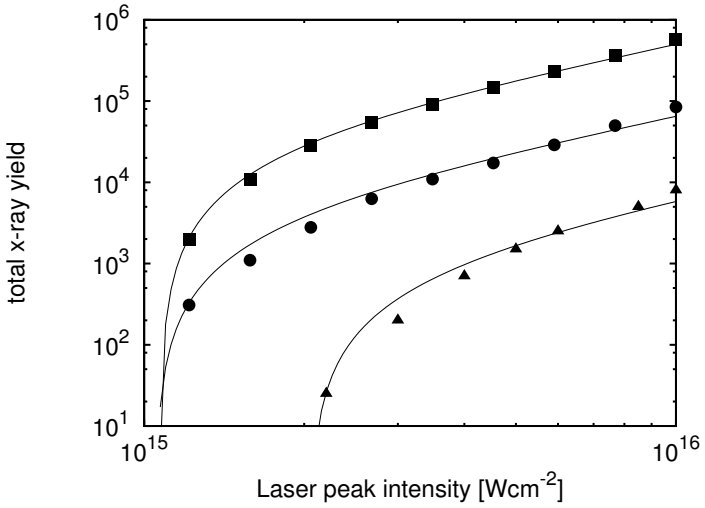

Figure 5.10: *Absolute x-ray yield for different laser peak intensities. The results for the cases with elastic electron-ion scattering and with dipole field (■, model 6) and without electron-ion scattering but with dipole field (●, model 5) are compared to the experimental results (▲). For each set of data, the solid line shows the evolution of the effective focal volume. For the case with scattering* $I_{th} = 1.07 \cdot 10^{15} \mathrm{Wcm}^{-2}$*, for the case without* $I_{th} = 1.05 \cdot 10^{15} \mathrm{Wcm}^{-2}$ *and for the experimental data* $I_{th} = 2.1 \cdot 10^{15} \mathrm{Wcm}^{-2}$*. The parameters are the same as in fig.5.9.*

Chapter 6

Electron-impact ionization

In the previous chapters the quasi-free electrons were only produced by over-barrier ionization, i.e. by field ionization of the cluster atoms (or ions). However, as the quasi-free electrons get heated very efficiently in the cluster after the first ionization burst, they soon have enough energy to ionize the cluster ions by electron-impact ionization. With this mechanism charge states q of the cluster ions can be reached that are not attainable by simple field ionization.

6.1 Implementation of electron-impact ionization

As our simulation treats the cluster ions as a homogeneous background charge, we take a stochastic approach to electron-impact ionization of the outer shells, just as we did for electron-ion scattering and production of K-shell vacancies. The probability that a given electron with energy E ionizes an ion during the time interval Δt is determined by the total cross-section for this process $\sigma_{ei}(q, E)$, the ionic target density ρ and the distance Δx traveled by the electron during the time Δt:

$$P_{ei} = \rho \sigma_{ei}(q, E) \Delta x \tag{6.1}$$

This probability is calculated for each time step and each simulated electron. A random number x_{rnd} between 0 and 1 is drawn and compared to P_{ei}. If $x_{rnd} > P_{ei}$ nothing happens. If $x_{rnd} < P_{ei}$, electron-impact ionization occurs, i.e. an additional quasi-free electron ($N_{MTC} \rightarrow N_{MTC} + 1$) is created at the position of the impact. The kinetic energy of the impacting electron is reduced by the binding energy of the outermost bound electron and is

then divided equally between the impacting and the ionized electron. The electrons are assumed to depart from each other enclosing an angle of 90°. This simple assumption for the energy transfer is made to reduce the influence of the transient states when elastic electron-ion scattering is neglected. However, the results obtained when including elastic electron-ion scattering are independent of the model chosen for the energy transfer. Furthermore we assume that the atom is instantaneously relaxed and the inner vacancies are filled by electrons from the outer shells. The cross section for electron-impact ionization depends on the energy of the impacting energy and the charge state of the target ion, for which the mean charge state $q = \frac{N_e}{N}$ is taken. For the dependence on these parameters different analytical models exist.

6.1.1 The Lotz formula

The semi-empirical Lotz formula [27] is widely used for estimations of the total cross-section for electron-impact ionization:

$$\sigma_{ei} = \sum_{i=1}^{N} a_i q_i \frac{\ln(E/W_i)}{EW_i} \{1 - b_i \exp[-c_i(E/W_i - 1)]\} \tag{6.2}$$

E is the kinetic energy of the impact electron, W_i is the binding energy of the electrons in the i-th subshell, q_i is the number of equivalent electrons in the $i-th$ subshell, a_i,b_i and c_i are empirical constants, that depend on the considered atom and its charge state. The sum extends over the $N = 3$ outermost populated subshells for argon. All electrons in the $2p$ or $3p$ shells are considered equivalent. Table 6.1 gives the values of a_i,b_i and c_i for Ar^{q+} with $q = 1, \ldots, 4$ [27]. For $q > 4$, one can assume $a_i = 2.17$a.u. and $b_i = 0$. Table 6.2 lists the binding energies of the different subshells for argon [25].

q	a_1	a_2	a_3	b_1	b_2	b_3	c_1	c_2	c_3
1	1.9	1.9	1.4	0.62	0.4	0.9	0.40	0.6	0.2
2	2.0	2.1	1.8	0.3	0.2	0.8	0.6	0.6	0.4
3	2.2	2.2	2.0	0.2	0	0.6	0.6	-	0.5
4	2.2	2.2	2.2	0	0	0.3	-	-	0.6

Table 6.1: *Parameters for the Lotz formula for* Ar^{q+}. a_i *is given in a.u.[27]*

The results from the Lotz formula are compared to experimental data for electron-impact ionization of argon in the upper graph of figure 6.1. The calculated data are of the right order of magnitude for all charge states.

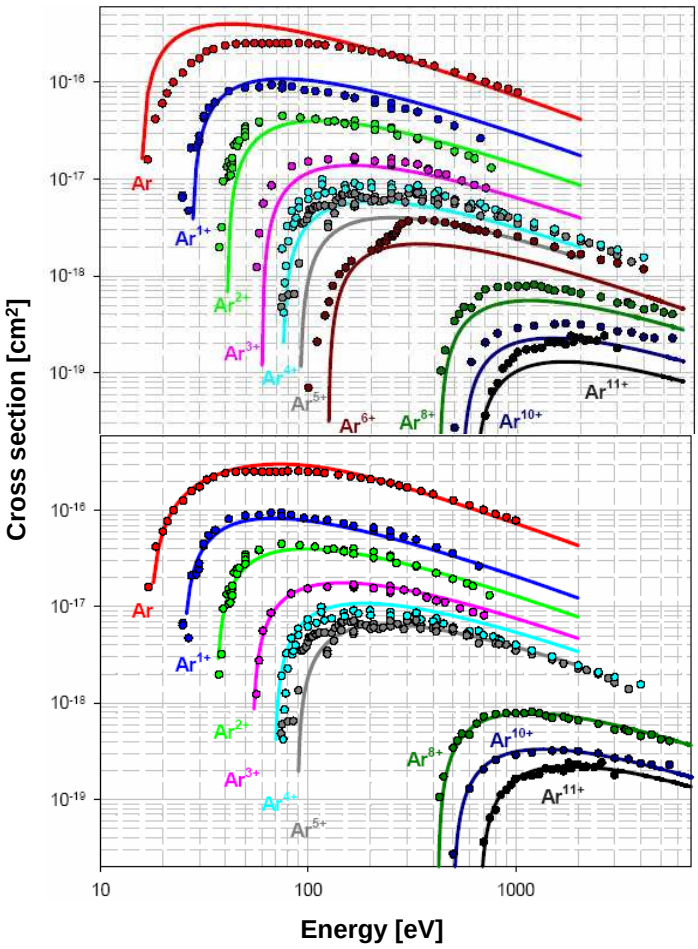

Figure 6.1: *Comparison of calculated (solid) electron-impact ionization cross sections for different charge states of argon with experimental data (circles) [12]. Upper graph: Lotz formula. Lower graph: equation (6.3).*

Label	Subshell	Binding Energy[a.u.]
K	1s	117.8
L_I	2s	12.0
L_{II}	$2p_{1/2}$	9.2
L_{III}	$2p_{3/2}$	9.1
M_I	3s	1.1
M_{II}	$3p_{1/2}$	0.6
M_{III}	$3p_{3/2}$	0.6

Table 6.2: *Electron binding energies for neutral argon[25].*

6.1.2 The Lotz formalism with fitted parameters

Even better agreement with the experimental data can be obtained by fitting the empirical parameters of the following equation [28, 12]:

$$\sigma_{ei}(E) = A\frac{\ln\left(E/W_q^*\right)}{EW_q^*} \qquad \text{for } E \geq W_q \tag{6.3}$$

q	W_q^*[a.u.]	W_q [a.u.]	A [a.u.]
1	0.92	1.02	6.76
2	1.32	1.49	6.76
3	1.98	2.20	6.76
4	2.76	2.76	5.55
5	2.94	3.34	5.79
8	15.51	15.53	18.35
10	18.38	19.84	11.11
11	24.62	22.72	13.04

Table 6.3: *Values of the parameters for equation 6.3 that provide the best fit to the experimental data [12].*

Table 6.3 shows the parameters for different charge states of argon [12]. The calculated data fits the experimental results much better (fig. 6.1) than the data obtained with unmodified Lotz formula. However the fit fails for $q = 6$ and the parameters for $q = 7, 9$ are not provided in [12]. This is due to resonant indirect processes, such as excitation autoionization, which become important at these charge states [29]. While for all other charge states formula (6.3) will be used in the simulation, for these charge states the results from the Lotz formula (6.2) will be taken.

6.2 Simulation results

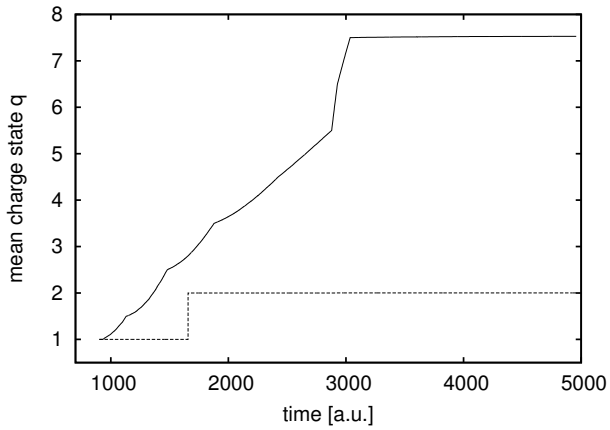

Figure 6.2: *Mean charge state $q = N_e/N$ of cluster ions. With electron-impact ionization (solid line, model 8), with field ionization only (dashed line, model 6). The cluster size is $N = 2.8 \cdot 10^5$ argon atoms, the laser intensity $I = 3.5 \cdot 10^{15}\mathrm{Wcm}^{-2}$, the pulse length $\tau = 60$fs and the wavelength $\lambda = 800$nm.*

The efficiency of electron-impact ionization can be seen in figure 6.2. The results were obtained by including electron-impact ionization in addition to the dipole field, the charging of the cluster and elastic electron-ion scattering (model 8). The electrons obeyed the equation of motion:

$$\ddot{\boldsymbol{x}} = -\boldsymbol{F}_L(t) - \boldsymbol{E}^{(0)}_{mean}(r,t) - \boldsymbol{E}^{(1)}_{mean}(\boldsymbol{r},t) + \boldsymbol{F}^{scatt}_{stoc} + \boldsymbol{F}^{eimp}_{stoc}. \tag{6.4}$$

The cluster size is again $N = 2.8 \cdot 10^5$ argon atoms. The laser intensity is $I = 3.5 \cdot 10^{15}\mathrm{Wcm}^{-2}$, the pulse length $\tau = 60$fs and the wavelength $\lambda = 800$nm. After the first ionization burst which happens by over-barrier ionization of the cluster atoms by the laser field, the electron-impact ionization sets in quickly within the first laser cycle. While field ionization would only allow to reach the charge state $q = 2$, electron-impact ionization leads to a mean charge state of up to $q = 7.5$. Field ionization plays no role after the first ionization burst as the ionization proceeds so quickly that the field ionization by over-barrier ionization or tunneling is no longer competitive. The steeper increase after $q = 5.5$ is an artefact of the electron impact cross section which is calculated from the Lotz formula for the charge states $q = 6$ and $q = 7$. Experimentally, high charge states (Ar^{12+} to Ar^{16+}) have been observed [12].

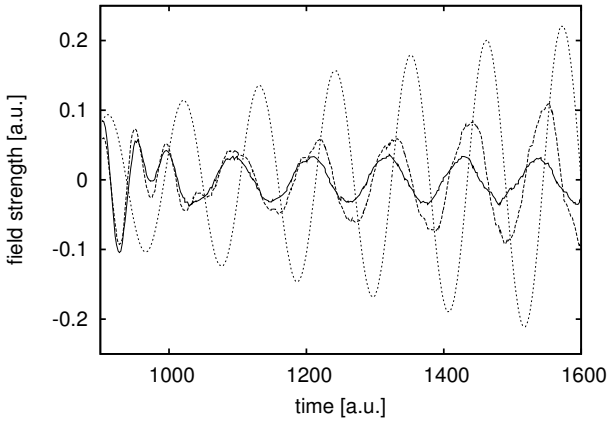

Figure 6.3: *Effective field inside the cluster with electron-impact ionization included (solid line, model 8) and with allowing only field ionization (dashed line, model 6). The dotted line is the laser field. The parameters are the same as in figure 6.2.*

However there is a lack of quantitative results for the mean charge state near the intensity threshold.

As the ionization proceeds, the number N_e of quasi-free electrons increases rapidly. The large number of slow electrons in the cluster has an important influence on the effective field inside the cluster (fig. 6.3). As N_e is larger, the eigenfrequency of the system $\omega_p^2 = N_e/R^3$ (see eq.(5.8)) increases and the amplitude of the dipole field E_p in the cluster approaches the laser field amplitude. The effective field inside the cluster is therefore even smaller than when only considering the dipole field. The smaller field causes the electrons to be heated less efficiently and the cluster charge therefore also increases slower than without electron-impact ionization (see fig.6.4).

6.2.1 K-shell vacancies

Because of the high number of electrons in the cluster and the slower heating due to the weak effective field, only a small fraction of the quasi-free electrons reaches the threshold for the production of K-shell vacancies. One therefore would have to perform the simulations with a very large number N_{MTC} of electrons. It is therefore more convenient to estimate the number N_K of K-shell vacancies produced by simply summing over the probabilities per time

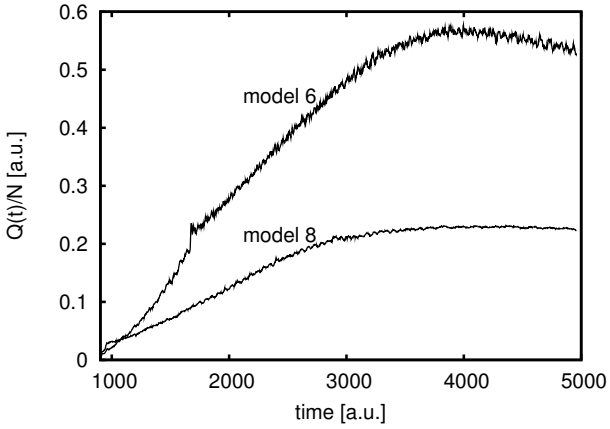

Figure 6.4: *Evolution of the cluster charge including electron-impact ionization (lower curve, model 8) and without (upper curve, model 6). The parameters are the same as in figure 6.2.*

step to produce a vacancy P_K:

$$N_K = \sum_{t_i=0}^{2\tau} P_K(t_i) \tag{6.5}$$

The error made by this method is not large as the number of electrons reaching energies where this probability is non zero is small, and as it is unlikely that an electron would produce a K-shell vacancy and then be heated back up again sufficiently to produce another one. Indeed as can be seen in figure 6.5 no more than 12 vacancies are produced even for $I = 10^{16}\mathrm{Wcm}^{-2}$. When neglecting elastic electron-ion scattering (model 7), about 10 times less K-shell vacancies are generated. In the case with field ionization only (model 6), about 100 vacancies per cluster were produced even for lower intensities.

6.2.2 X-ray yield

For neutral argon the fluorescence yield is $\omega_f \simeq 0.11$. For charged argon the fluorescence yield increases. At a mean charge state of $q = 14.5$ it is about $\omega_f \simeq 0.35$ [12]. As the mean charge state of the argon ions is now in the range of $q = 8$, we assume a fluorescence yield of $\omega_f \simeq 0.2$. The yields without elastic electron-ion scattering (model 7) are too small compared to the experimental results (fig. 6.6). The yields obtained when taking the unmodified Lotz formula for calculating the electron impact cross section are even much lower due to an even faster ionization of the cluster ions.

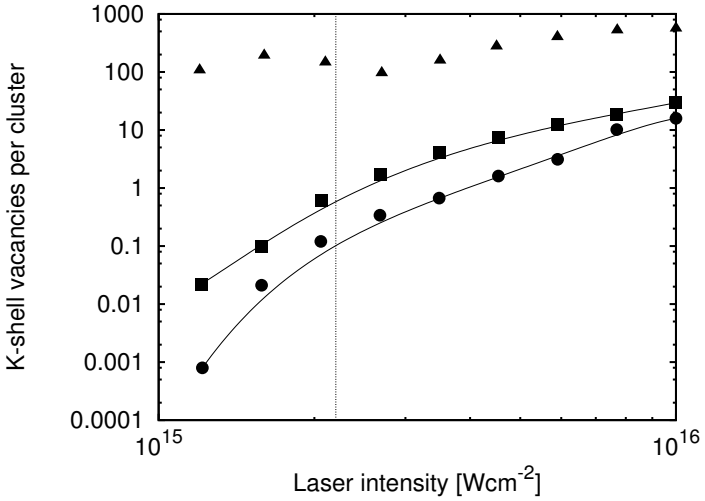

Figure 6.5: *Number of produced K-shell vacancies for different laser peak intensities. With elastic electron-ion scattering and with electron-impact ionization (■, model 8), with electron-impact ionization but without elastic electron-ion scattering (●, model 7) and with electron-ion scattering but with field ionization only (no electron-impact ionization) (▲, model 6) are compared (the solid lines are shown to guide the eye). The vertical dashed line marks the experimental intensity threshold for x-ray production. The size of the argon cluster was* $N = 2.8 \cdot 10^5$. *The laser duration was* $\tau = 60$fs, *the wavelength* $\lambda = 800$nm.

The simulation of the cluster is thus very sensitive to the implementation of electron-impact ionization as it has such a large influence on the effective field. However when using the modified parameters for calculating the electron-impact ionization and including elastic electron-ion scattering (model 8), the agreement between simulation and experiments is very good and the simulation results lie well within the experimental error (fig. 6.7). This again illustrates the importance of including elastic electron-ion scattering as an efficient heating mechanism in the simulation.

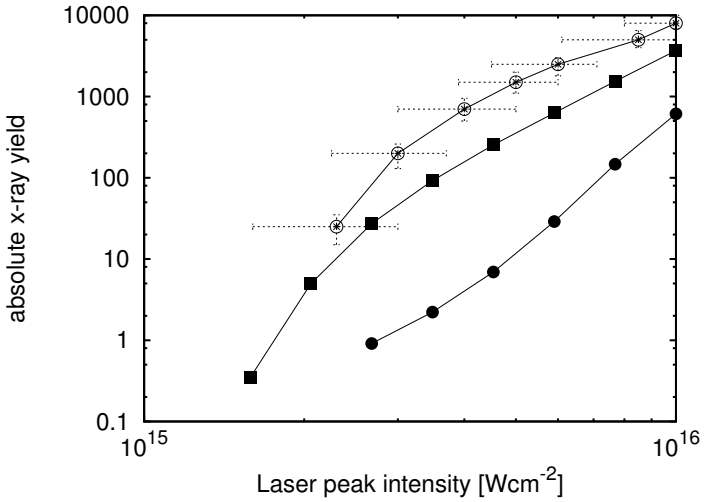

Figure 6.6: *Absolute x-ray yield for different laser peak intensities. Without elastic electron-ion scattering (■, model 7) and experimental results (◯). The results when using the Lotz formula for the ionization cross section are also shown (●, model 8 with Lotz formula). The parameters are the same as in fig.6.5.*

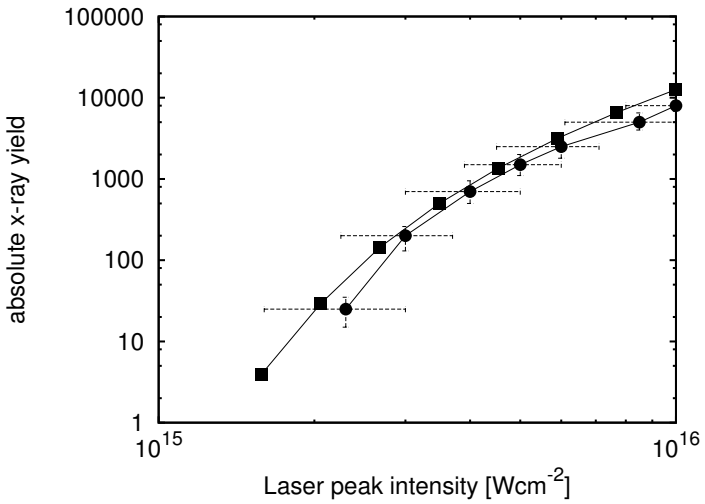

Figure 6.7: *Absolute x-ray yield for different laser peak intensities. The results of the simulation with elastic electron-ion scattering (■, model 8) are compared to the experimental results (●). The parameters are the same as in fig.6.5.*

Chapter 7

Parameter dependence of the x-ray yields

In this chapter we will test the dependence of the intensity threshold and the x-ray yield on different parameters. We will vary the pulse duration, the wavelength of the laser, the cluster size and the polarization of the laser. The simulation explores the intensity region near the threshold for x-ray production. However, many experimental studies with a fixed peak intensity, are carried out at high intensities ($I > 10^{16}$), like the evolution of the absolute x-ray yield with the backing pressure or the pulse duration. These high intensities would make the simulation computationally expensive as the higher forces acting on the electrons call for a smaller time step Δt. Moreover, because of the intensity distribution in the focal volume, many runs at different intensities are needed for each set of parameters. The same problems arise if in the experiment not the laser intensity but the laser energy is kept constant. We therefore restrict the parameter studies to the intensity region near the threshold.

7.1 Pulse length dependence

The study of the evolution of the x-ray yields with the pulse length can become computationally expensive as the shortest pulse durations for which there are experimental data are $\tau \simeq 60$fs. For longer pulses, the simulations are more demanding. Figure 7.1 shows the evolution of the x-ray yields for three different laser pulse durations. The threshold for the x-ray production is clearly shifted to lower intensities as the pulses become longer. This is in agreement with the experimental observations. Simulation results show that the rate of production of quasi-free electrons by electron impact ionization is

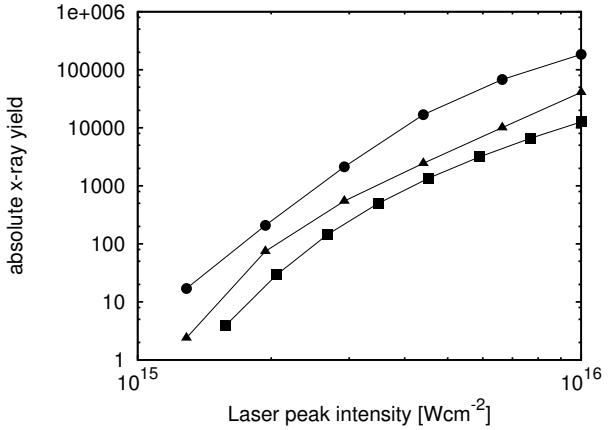

Figure 7.1: *Absolute x-ray yields for different laser peak intensities and different pulse durations:* $\tau = 60$fs (■), $\tau = 90$fs (▲) *and* $\tau = 120$fs (●). *The cluster size is* $N = 2.8 \cdot 10^5$ *argon atoms. The wavelength of the laser is* $\lambda = 800$nm.

largely independent of the pulse duration. However if the pulse is longer the ionized electrons have more time to get heated, explaining the higher x-ray yields.

7.2 Wavelength dependence

The experiments have also been conducted for laser pulses with a wave length of $\lambda = 400$nm. However the results for different wavelengths have to be compared with care as the shorter wavelengths are obtained by doubling the frequency of a pulse with 800nm with a crystal. As a consequence the pulse duration is also increased: a pulse with $\tau = 50fs$ at 800 nm is transformed into a pulse with $\tau = 130fs$ and 400 nm. Therefore, to be able to investigate pulse durations shorter than $\tau = 130fs$ with 400nm, a numerical analysis of the measurements is necessary. This analysis of the experimental data showed that at same peak intensity and laser duration the probability for producing K-shell vacancies should be independent of the wave length. Differences in the measured yields arise only from a focal volume of the laser that is smaller at 400 nm.

Figure 7.2 shows the simulation results for the number of produced K-shell vacancies per cluster for 800 nm and 400 nm at the same pulse length of $\tau = 60$fs and cluster size $N = 2.8 \cdot 10^5$. In the case of $\lambda = 400$nm more vacancies are produced. This is due to the fact that because of the higher

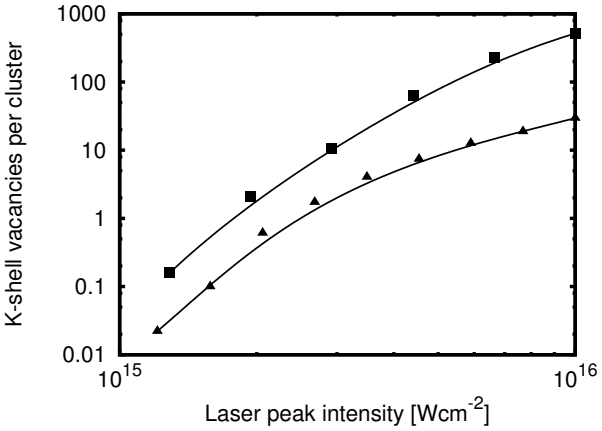

Figure 7.2: *Number of produced K-shell vacancies per cluster for a laser pulse with a wavelength of 800 nm (▲) and 400 nm (■) (the solid line is to guide the eye). The cluster size is* $N = 2.8 \cdot 10^5$ *argon atoms and the pulse duration* $\tau = 60$fs.

laser frequency, the resonance condition $\omega_p^2 = N_e/R^3 = \omega^2$ is now met during the laser pulse. Figure 7.3 shows the evolution of the eigenfrequency ω_p during the laser pulse. In the second half of the pulse, as the cluster expands rapidly, it becomes equal to the laser frequency ω. Near this resonance the mean kinetic energy of the electrons increases rapidly by nearly a factor 6. This additional heating due to the resonance explains the higher number of produced K-shell vacancies. This is in disagreement with the experimental results, which showed that the vacancy yield should be independent from the laser wavelength. However in this simulation the cluster expansion is overestimated, as the screening of the ion charge by the quasi-free electrons surrounding it, is not considered. If the expansion of the cluster is slower, the resonance could be avoided, resulting in less produced K-shell vacancies.

7.3 Cluster size dependence

Figure 7.4 shows the simulation results for several cluster sizes. The absolute yields increase with larger cluster sizes which is in qualitative agreement with the experimental results. No noticeable change in the position of the threshold can be seen. Presently no experimental data are available for the evolution of the intensity threshold with different backing pressures.

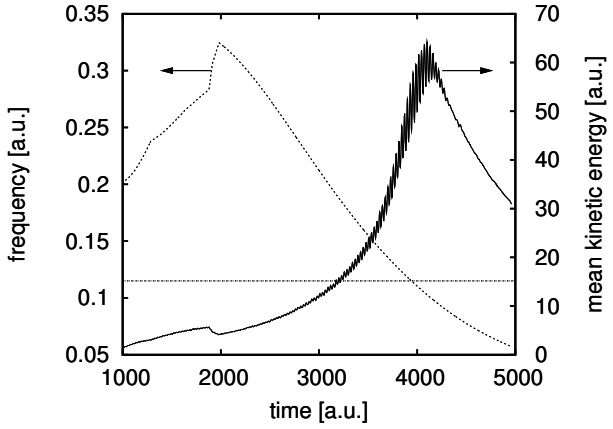

Figure 7.3: *Evolution of the eigenfrequency ω_p (dashed line, left axis) during the laser pulse. The laser frequency ω is indicated by the horizontal dotted line. The mean kinetic energy of the electrons is also shown (solid line, right axis). The cluster size is $N = 2.8 \cdot 10^5$ argon atoms, the intensity $I = 4.4 \cdot 10^{15}\mathrm{Wcm}^2$, the wavelength $\lambda = 400nm$ and the pulse duration $\tau = 60\mathrm{fs}$.*

7.4 Laser polarization

To compare results for circular and linear polarizations of the laser, we introduce a factor $1/\sqrt{2}$ in the laser field amplitude of the circular light to ensure that the energy of the laser field is equal for the two polarizations. Experiments show that at equal laser energy the absolute x-ray yields are a factor 0.81 smaller for circular polarization than for linear polarization. This factor can be reproduced very well by the simulations as shown in figure 7.5.

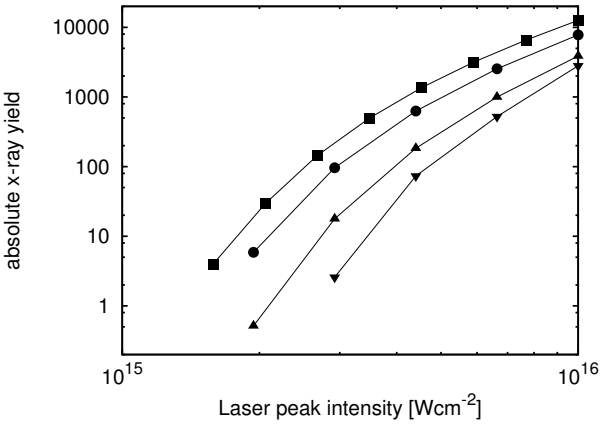

Figure 7.4: *Absolute x-ray yields for different laser peak intensities and different cluster sizes. from top to bottom:* $N = 2.8{\cdot}10^5$ *(*$P = 40$bar*),* $N = 1.7{\cdot}10^5$ *(*$P = 30$bar*),* $N = 8.1 \cdot 10^4$ *(*$P = 20$bar*) and* $N = 5.4 \cdot 10^4$ *(*$P = 16$bar*). The wavelength of the laser is* $\lambda = 800$nm *and the pulse duration is* $\tau = 60$fs.

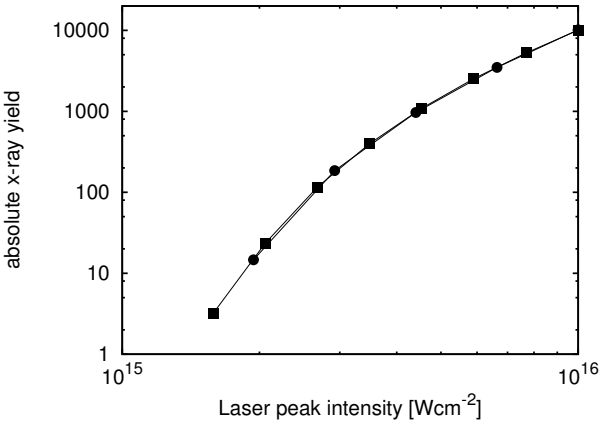

Figure 7.5: *Absolute x-ray yields for different laser peak intensities for a linear (■) and a circular (•) polarized laser. The results for the linear polarization are weighted with a factor 0.8 to show the correspondence with the experimental results. The cluster size is* $N = 2.8 \cdot 10^5$ *argon atoms. The wavelength of the laser is* $\lambda = 800$nm *and the pulse duration is* $\tau = 60$fs.

Chapter 8

Summary

In this work we studied the production of hot electrons in rare gas clusters irradiated by intense short laser pulses. This study was motivated by experimental results [1, 2, 13], which showed an unexpectedly low laser intensity threshold for the emission of x-rays by cluster atoms. This indicates that efficient heating mechanisms are at play inside a cluster, which make the quasi-free electrons reach energies sufficient for the production of K-shell vacancies by electron-impact ionization. To test the influence of different physical mechanisms on the heating of the electrons, we created a simple Monte Carlo simulation of the cluster. The simulation results showed that:

- elastic electron-ion scattering is a very efficient heating mechanism for the electrons, raising the number of produced K-shell vacancies by a factor 2-3,
- the charging of the cluster contributes also to the heating of the electrons as it diminishes the potential inside the cluster and thus increases the kinetic energy,
- the polarization effects due to the laser create a uniform electric field inside the cluster which acts against the laser field and thus decelerates the electrons,
- electron-impact ionization of the cluster ions is highly effective and explains the high charge states observed experimentally.

When considering all the effects mentioned above, the x-ray yields predicted by the simulation lie within the error estimates of the experimental results. We also probed the dependence of the x-ray yield on the pulse length, the

wavelength, the cluster size and the laser polarization. A quantitative comparison with the experimental findings was often not possible, as the simulation of the high laser intensities, with which many experiments were conducted, become computationally expensive. The general trends could, however, be reproduced by the simulations, even though the simulations showed resonance effects in certain parameter ranges which were not seen experimentally.

Appendix A

Atomic units

A.1 Conversion to SI units [30]

1 a.u. of:

charge	$1.60217653(14) \cdot 10^{-19}$ C
mass	$9.1093826(16) \cdot 10^{-31}$ kg
action	$1.05457168(18) \cdot 10^{-34}$ Js
length	$0.5291772108(18) \cdot 10^{-10}$ m
energy	$4.35974417(75) \cdot 10^{-18}$ J
time	$2.418884326505(16) \cdot 10^{-17}$ s
force	$8.2387225(14) \cdot 10^{-8}$ N
velocity	$2.1876912633(73) \cdot 10^{6}$ ms^{-1}
momentum	$1.99285166(34) \cdot 10^{-24}$ kgms^{-1}
electric field	$5.14220642(44) \cdot 10^{11}$ Vm^{-1}
electric dipole moment	$8.47835309(73) \cdot 10^{-30}$ Cm

A.2 Useful relations

Energy conversion:

$$1\text{a.u.} = 27.2113961\text{eV} \tag{A.1}$$

The rotational frequency ω in a.u. from the wavelength in nm:

$$\omega[\text{a.u.}] = \frac{45.563353}{\lambda[\text{nm}]} \tag{A.2}$$

Field amplitude A in a.u. from intensity I in Wcm^{-2}:

$$A[\text{a.u.}] = 5.3380248 \cdot 10^{-9} \sqrt{I[\text{Wcm}^{-2}]} \tag{A.3}$$

Appendix B

The velocity Verlet algorithm

The velocity Verlet algorithm is a method to propagate the equation of motion of a particle. The difference to the Verlet algorithm [31] is that the velocity is also evaluated. Position, velocity and acceleration at time $(t+\Delta t)$ are obtained from the force F and from the same quantities at time t in the following way:

$$x(t+\Delta t) = x(t) + v(t)\Delta t + a(t)\frac{\Delta t^2}{2} \tag{B.1}$$

$$v(t+\frac{\Delta t}{2}) = v(t) + a(t)\frac{\Delta t}{2} \tag{B.2}$$

$$a(t+\Delta t) = \frac{F(x(t+\Delta t), t+\Delta t)}{m} \tag{B.3}$$

$$v(t+\Delta t) = v(t+\frac{\Delta t}{2}) + a(t+\Delta t)\frac{\Delta t}{2} \tag{B.4}$$

With this method, the error in the position of the particle is only of the order of Δt^4.

Appendix C

Scattering in cartesian coordinates

When considering a scattering event, the scattering angles $(\theta_{scatt}, \phi_{scatt})$ are given relative to the velocity $\boldsymbol{v}$ of the incident particle. To get the velocity $\boldsymbol{v'}$ of the particle after the scattering event in the cartesian coordinate system (x, y, z), it is convenient to consider the coordinate system (x', y', z') where the z' direction is the direction of $\boldsymbol{v}$. Let this direction be:

$$\boldsymbol{v} = \begin{pmatrix} r\cos\phi\sin\theta \\ r\sin\phi\sin\theta \\ r\cos\theta \end{pmatrix} \tag{C.1}$$

The directions of x' and y' have only to be orthogonal to z'. For convenience let us consider the system (x', y', z') which is obtained from the original system (x, y, z) by performing a rotation around the z axis with an angle of $-(\pi/2 - \phi)$ followed by a rotation around the x' axis with an angle of $-\theta$. In this new coordinate system the velocity of the scattered particle is given by:

$$\boldsymbol{v'} = \begin{pmatrix} r\cos\phi_{scatt}\sin\theta_{scatt} \\ r\sin\phi_{scatt}\sin\theta_{scatt} \\ r\cos\theta_{scatt} \end{pmatrix} \tag{C.2}$$

To transform this velocity back to the original system (x, y, z), one has to invert the rotations described above. The transformation matrix that describes

the transition from (x', y', z') back to (x, y, z) is therefore:

$$\begin{aligned} M &= \begin{pmatrix} \sin\phi & \cos\phi & 0 \\ -\cos\phi & \sin\phi & 0 \\ 0 & 0 & 1 \end{pmatrix} \begin{pmatrix} 1 & 0 & 0 \\ 0 & \cos\theta & \sin\theta \\ 0 & -\sin\theta & \cos\theta \end{pmatrix} \\ &= \begin{pmatrix} \sin\phi & \cos\theta\cos\phi & \cos\phi\sin\theta \\ -\cos\phi & \sin\phi\cos\theta & \sin\theta\sin\phi \\ 0 & -\sin\theta & \cos\theta \end{pmatrix} \end{aligned} \tag{C.3}$$

The evaluation of $M\boldsymbol{v'}$ gives the coordinates of $\boldsymbol{v'}$ in the original basis (x, y, z).

Appendix D

The Poisson equation on an axisymmetrical grid with cells of equal volume.

D.1 The $r - \theta$ grid

When confronted with a problem that is rotationally symmetric around an axis (for example the z-axis), it is useful to work in axisymmetrical coordinates (r, θ). The relationship to the cartesian coordinates is:

$$r = \sqrt{x^2 + y^2 + z^2} \tag{D.1}$$

$$\cos(\theta) = \frac{z}{\sqrt{x^2 + y^2 + z^2}} \tag{D.2}$$

One can then discretise a sphere with radius R and volume V with a $r - \theta$ grid with N_r steps in r and N_θ steps in θ:

$$r_i = \sum_{k=1}^{i} \Delta r_k \tag{D.3}$$

$$\theta_1 = \frac{1}{2}\Delta\theta_1 \tag{D.4}$$

$$\theta_j = \sum_{k=1}^{j-1} \Delta\theta_k + \frac{1}{2}\Delta\theta_j \tag{D.5}$$

As can be seen in figure D.1, the discretization steps Δr_k and $\Delta\theta_k$ are not constant, but are chosen to assure that the cells all have equal volume

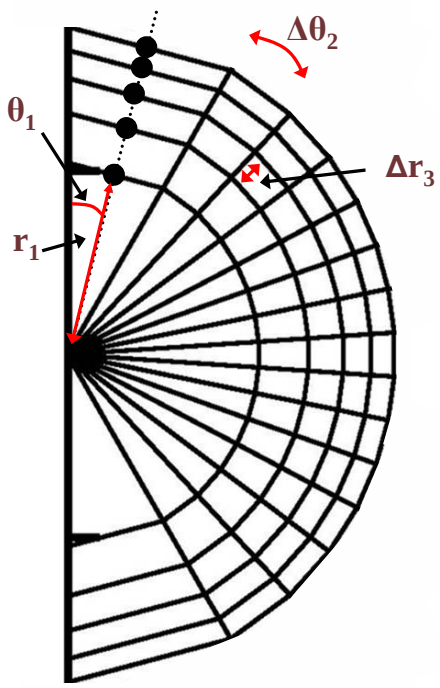

Figure D.1: $r-\theta$ *discretization of a sphere. Each cell should be seen as the volume obtained when rotating the section around the z-axis. These cells all have equal volume.*

$V_{i,j} = \frac{V}{N_r N_\theta}$. Δr_k can be determined by recursion when one demands that the spherical shell between r_k and r_{k+1} has a volume of $\frac{V}{N_r}$:

$$\Delta r_1 = \sqrt[3]{\frac{1}{N_r}} R \tag{D.6}$$

$$\Delta r_k = \sqrt[3]{\frac{k}{N_r}} R - \sum_{l=1}^{k-1} \Delta r_l \tag{D.7}$$

The $\Delta\theta_k$ are also given recursively:

$$\Delta\theta_1 = \arccos(1 - \frac{2}{N_\theta}) \tag{D.8}$$

$$\Delta\theta_k = \arccos(1 - \frac{2k}{N_\theta}) - \sum_{l=1}^{k-1} \Delta\theta_l \tag{D.9}$$

The cell (i, j) corresponding to a given pair (r, θ) is determined by:

$$i = \left\lceil N_r \frac{r^3}{R^3} \right\rceil \tag{D.10}$$

$$j = \left\lceil \frac{1 - \cos\theta}{2} N_\theta \right\rceil \tag{D.11}$$

with $\lceil x \rceil$ denoting the smallest integer larger than x.

D.2 The discretized Poisson equation

The Poisson equation gives the relationship between the charge density $\rho(r, \theta)$ and the electric potential $u(r, \theta)$. In axisymmetrical coordinates (r, θ) it has the following form:

$$\frac{\partial^2 u}{\partial r^2} + \frac{2}{r}\frac{\partial u}{\partial r} + \frac{1}{r^2}\frac{\partial^2 u}{\partial \theta^2} + \frac{\cos(\theta)}{r^2 \sin(\theta)}\frac{\partial u}{\partial \theta} = -4\pi\rho(r, \theta) \tag{D.12}$$

When discretising the space as described in the previous section, the differential operators become finite difference operators:

$$\frac{\partial u}{\partial r}(r, \theta) = \frac{u_{i+1,j} - u_{i-1,j}}{\Delta r_{i+1} + \Delta r_i} \tag{D.13}$$

$$\frac{\partial u}{\partial \theta}(r, \theta) = \frac{u_{i,j+1} - u_{i,j-1}}{\frac{\Delta\theta_{j+1}}{2} + \Delta\theta_j + \frac{\Delta\theta_{j-1}}{2}} \tag{D.14}$$

The discretized Poisson equation has the general form:

$$a_{i,j}u_{i+1,j} + b_{i,j}u_{i-1,j} + c_{i,j}u_{i,j+1} + d_{i,j}u_{i,j-1} + e_{i,j}u_{i,j} = f_{i,j} \tag{D.15}$$

The coefficients a, b, c, d, e and f are determined by the form of the finite

difference operators:

$$a_{i,j} = \frac{2}{\Delta r_{i+1} + \Delta r_i}\left(\frac{1}{r_i} + \frac{1}{\Delta r_{i+1}}\right) \tag{D.16}$$

$$b_{i,j} = \frac{2}{\Delta r_{i+1} + \Delta r_i}\left(-\frac{1}{r_i} + \frac{1}{\Delta r_i}\right) \tag{D.17}$$

$$c_{i,j} = \frac{1}{r_i^2\left(\frac{\Delta\theta_{j+1}}{2} + \Delta\theta_j + \frac{\Delta\theta_{j-1}}{2}\right)}\left(\frac{\cos\theta_j}{\sin\theta_j} + \frac{4}{\Delta\theta_{j+1} + \Delta\theta_j}\right) \tag{D.18}$$

$$d_{i,j} = \frac{1}{r_i^2\left(\frac{\Delta\theta_{j+1}}{2} + \Delta\theta_j + \frac{\Delta\theta_{j-1}}{2}\right)}\left(-\frac{\cos\theta_j}{\sin\theta_j} + \frac{4}{\Delta\theta_j + \Delta\theta_{j-1}}\right) \tag{D.19}$$

$$e_{i,j} = -\frac{2}{\Delta r_{i+1} + \Delta r_i}\left(\frac{1}{\Delta r_{i+1}} + \frac{1}{\Delta r_i}\right) - \frac{4}{r_i^2\left(\frac{\Delta\theta_{j+1}}{2} + \Delta\theta_j + \frac{\Delta\theta_{j-1}}{2}\right)} \cdot \left(\frac{1}{\Delta\theta_{j+1} + \Delta\theta_j} + \frac{1}{\Delta\theta_j + \Delta\theta_{j-1}}\right) \tag{D.20}$$

$$f_{i,j} = -4\pi\rho_{i,j} \tag{D.21}$$

To assure the continuity at the symmetry axis, one has to request:

$$\frac{\partial u(r,0)}{\partial\theta} = \frac{\partial u(r,\pi)}{\partial\theta} = 0 \tag{D.22}$$

This translates into:

$$c_{i,1} = \frac{4}{r_i^2\left(\frac{\Delta\theta_2}{2} + \frac{3\Delta\theta_1}{2}\right)}\left(\frac{1}{\Delta\theta_2 + \Delta\theta_1} + \frac{1}{2\Delta\theta_1}\right) \tag{D.23}$$

$$c_{i,N_\theta} = 0 \tag{D.24}$$

$$d_{i,1} = 0 \tag{D.25}$$

$$d_{i,N_\theta} = c_{i,1} \tag{D.26}$$

Thanks to the choice for the discretization of r, there is no need for a pole condition at $r = 0$ as:

$$b_{1,j} = 0 \tag{D.27}$$

The boundary condition in r is simply given by fixing the potential at the boundary:

$$u_{N_r,j} = u^{(0)}_{N_r,j} \tag{D.28}$$

This boundary value problem can now be solved numerically, for example by successive overrelaxation (SOR) [32].

Acknowledgements

I'd like to express my gratitude to all, who made the completion of this work possible, both with profound knowledge and personal support. In particular, I would like to thank Joachim Burgdörfer and Nina Rohringer for their guidance and their ever-open ear. For fruitful discussions and an experimental insight my thanks go to Dominique Vernhet and Emily Lamour. Finally, I deeply thank my family and friends for their encouragement, sometimes necessary distraction and unbroken optimism.

Bibliography

[1] L. Adoui et al., Nucl.Instr. and Meth. B 205, 341 (2003)

[2] C. Prigent et al., J.Phys. IV France 108, 191 (2003)

[3] T. Ditmire T. Donnelly, A.M. Rubenchik, R.W. Falcone, M.D. Perry, Phys. Rev. A 53, 3379 (1996)

[4] I. Last, J. Jortner, J. Phys. Chem A. 102,9655 (1998)

[5] I. Last, J. Jortner, Phys. Rev. A 60, 2215 (1999)

[6] C. Rose-Petruck, K.J. Schafer, K.R. Wilson, C.P.J. Barty, Phys. Rev. A 55, 1182 (1997)

[7] U. Saalmann, J.M. Rost, Phys. Rev. Lett. 91, 223401 (2003)

[8] C. Siedschlag, J.M. Rost, Phys. Rev. A 67 (2003) 013404

[9] C. Jungreuthmayer, M. Geissler, J. Zanghellini, T. Brabec, Phys. Rev. Lett. 92, 133401 (2004)

[10] M.B. Smirnov, W. Becker, Phys. Rev. A 69, 013201 (2004)

[11] S. Dobosz et al., Phys. Rev. A 56 R1 (1997)

[12] Christophe Prigent, L'émission X : un outil et une sonde pour l'interaction laser-agrégats, Thèse de doctorat (07 décembre 2004), Groupe de Physique des Solides, Université Pierre et Marie Curie, Paris VI, http://tel.ccsd.cnrs.fr/documents/archives0/00/00/81/59/index_fr.html

[13] Proceedings of the 12th international conference on the physics of highly charged ions (HCI 2004) to be published in Nucl. Instr. and Meth. B

[14] E. Fermi, Phys. Rev. **75**, 1169 (1949)

[15] J. Burgdörfer, J.Wang, R.H. Ritchie, Phys. Scr. 44, 391 (1991)

[16] R. Santra, C.H. Greene, Phys. Rev. Lett. 91, 233401 (2003)

[17] M.V. Ammosov, N.B. Delone, V.P. Krainov, Sov. Phys. JETP 64, 1191 (1986)

[18] H. Bethe, E. Salpeter, Quantum Mechanics of One- and Two-Electron Atoms, Springer, Berlin (1975)

[19] M. Liu, At. Data and Nucl. Data. Tables 76, 213 (2000)

[20] F. Salvat, R. Mayol, Comput. Phys. Commun. 74, 358 (1993)

[21] R.H. Garvey, C.H. Jackman, A.E.S. Green, Phys. Rev. A 12, 1144 (1975)

[22] N. F. Mott and H. S. W. Massey, The Theory of Atomic Collisions, Oxford Univ. Press, Oxford (1933)

[23] H. Haberland Clusters of atoms, molecules I : theory, experiment, and clusters of atoms. Springer-Verlag, Berlin New-York (1994)

[24] V.P. Krainov, A.S. Roshchupkin J. Phys. B: At. Mol. Opt. Phys. 34, L297 (2001)

[25] Webelements [http://www.webelements.com/]

[26] E.M. Purcell, Berkeley Physics Course, Vol 2, McGraw-Hill, New York (1965)

[27] W.Lotz, Z. Phys. 216, 241 (1968)

[28] A. Mueller, E. Salzborn, R. Frodl, R.Becker, H.Klein, H. Winter, J. Phys. B: At. Mol. Opt. Phys. 13, 1877 (1980)

[29] S.S. Tayal, R.J.W. Henry, Phys. Rev. A 33, 38253831 (1986)

[30] P. J. Mohr and B. N. Taylor, The 2002 CODATA Recommended Values of the Fundamental Physical Constants, Web Version 4.0, available at physics.nist.gov/constants

[31] L. Verlet, Phys. Rev. 159, 98 (1967)

[32] William H. Press, Numerical Recipes in Fortran 77: The Art of Scientific Computing, Cambridge University Press (1992)